Improved accuracy in high-frequency AC transport measurements in pulsed high magnetic fields

Hiroyuki Mitamura, Ryuta Watanuki, Erik Kampert, Tobias Förster, Akira Matsuo, Takahiro Onimaru, Norimichi Onozaki, Yuta Amou, Kazuhei Wakiya, Keisuke T. Matsumoto, Isao Yamamoto, Kazuya Suzuki, Sergei Zherlitsyn, Joachim Wosnitza, Masashi Tokunaga, Koichi Kindo, and Toshiro Sakakibara

View Online   Export Citation   CrossMark

ARTICLES YOU MAY BE INTERESTED IN

Sub-kelvin temperature management in ion traps for optical clocks
Review of Scientific Instruments **91**, 111301 (2020); https://doi.org/10.1063/5.0024693

Multiprobe scanning probe microscope using a probe-array head
Review of Scientific Instruments **91**, 123702 (2020); https://doi.org/10.1063/5.0015897

An automated setup to measure the linear and nonlinear magnetic ac-susceptibility down to 4 K with higher accuracy
Review of Scientific Instruments **91**, 123905 (2020); https://doi.org/10.1063/5.0029095
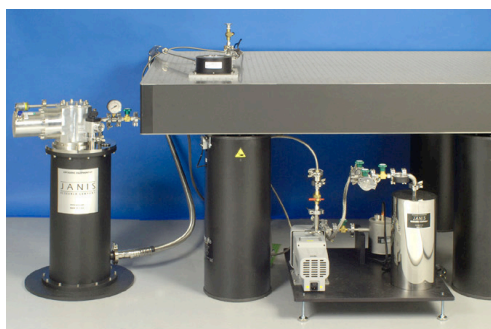
Improved accuracy in high-frequency AC transport measurements in pulsed high magnetic fields

View Online   Export Citation   CrossMark

Hiroyuki Mitamura,[1,a] [iD] Ryuta Watanuki,[2] [iD] Erik Kampert,[3,b] [iD] Tobias Förster,[3] Akira Matsuo,[1]
Takahiro Onimaru,[4] [iD] Norimichi Onozaki,[2] Yuta Amou,[2] Kazuhei Wakiya,[4,c] Keisuke T. Matsumoto,[4,d]
Isao Yamamoto,[2] Kazuya Suzuki,[2] Sergei Zherlitsyn,[3] Joachim Wosnitza,[3,5] Masashi Tokunaga,[1] [iD]
Koichi Kindo,[1] and Toshiro Sakakibara[1]

AFFILIATIONS

[1] Institute for Solid State Physics, The University of Tokyo, Kashiwa 277-8581, Japan
[2] Faculty of Engineering, Yokohama National University, Yokohama 240-8501, Japan
[3] Hochfeld-Magnetlabor Dresden (HLD-EMFL) and Würzburg-Dresden Cluster of Excellence ct.qmat,
   Helmholtz-Zentrum Dresden-Rossendorf, 01328 Dresden, Germany
[4] Graduate School of Advanced Science and Engineering, Hiroshima University, Higashi-Hiroshima 739-8530, Japan
[5] Institut für Festkörper- und Materialphysik, TU Dresden, 01062 Dresden, Germany

[a] Author to whom correspondence should be addressed: mitamura@issp.u-tokyo.ac.jp
[b] Present address: WMG, University of Warwick, Coventry CV4 7AL, UK.
[c] Present address: The Center for Rare Earths Research, Muroran Institute of Technology, Muroran 050-8585, Japan.
[d] Present address: Graduate School of Science and Engineering, Ehime University, Matsuyama 790-8577, Japan.

ABSTRACT

We show theoretically and experimentally that accurate transport measurements are possible even within the short time provided by pulsed magnetic fields. For this purpose, a new method has been devised, which removes the noise component of a specific frequency from the signal by taking a linear combination of the results of numerical phase detection using multiple integer periods. We also established a method to unambiguously determine the phase rotation angle in AC transport measurements using a frequency range of tens of kilohertz. We revealed that the dominant noise in low-frequency transport measurements in pulsed magnetic fields is the electromagnetic induction caused by mechanical vibrations of wire loops in inhomogeneous magnetic fields. These results strongly suggest that accurate transport measurements in short-pulsed magnets are possible when mechanical vibrations are well suppressed.

I. INTRODUCTION

Pulsed magnets allow us to reach magnetic fields much larger than available when using static-field magnets. Various physical properties (magnetization, ESR,[1,2] NMR,[3] neutron diffraction,[4] x-ray diffraction,[5] x-ray absorption,[6] magnetic torque,[7] magnetostriction,[8–11] magnetocaloric effect,[12,13] heat capacity,[14,15] imaging,[16] cyclotron resonance,[17,18] ultrasound,[19,20] electric polarization,[21–23] and so on) have been measured by using pulsed magnetic fields.

Especially in transport measurements, much research on semiconductor, semimetals,[24,25] metal to insulator transitions,[26] and superconductors[27,28] has been carried out using pulsed magnets. On the other hand, magnetoresistance measurements of highly conductive metals have not been performed very vigorously, although this has been enabled by using highly sophisticatedly cut samples.[29–31] This is because of the challenges to achieve a sufficiently high resolution.[32,33] In other words, the integration time in pulsed magnetic fields is significantly shorter than that for static magnetic fields,

and the signal is hidden in the noise inherent to generating pulsed magnetic fields.

Until now, a usual way for achieving a better resolution is to increase the pulse-duration time, i.e., to increase the integration time. This means, however, to increase the size of the power supply and the magnet, which required substantial initial investment and maintenance costs. Since a large amount of energy dissipates inside the magnet, the time required to cool down the magnet becomes long, restricting the number of pulses per experimental run significantly.

To overcome this difficulty, we propose a different approach. The improved accuracy in high-frequency AC transport measurements is promoted by an advanced concept of numerical phase detection, which enables demodulation within a short time and at a low frequency by integrating over an integer number of periods. If mechanical vibrations can be suppressed effectively, long pulse durations are not necessarily required for highly accurate measurements.

We will first show the basic principles of our method in Sec. II. Next, pulsed-field measurements in Yokohama (Sec. III A), Dresden (Sec. III B), and Kashiwa (Sec. III C) will be described. In Secs. III A–III C, we will show that low-noise measurements can be made even in a short time, our method of correcting the phase shift is appropriate, and verify the frequency dependence and how to solve issues related to the simultaneous measurements of multiple samples.

II. FUNDAMENTALS

Here, we explain the basic method of high-resolution electrical transport measurements in pulsed magnetic fields established by the authors. The improvement achieved using our measurement method is largely due to the introduction of a low-frequency AC method by numerical phase detection. Section II A explains the basic principle of the numerical phase detection method and the reason for its efficiency in measurements in pulsed magnetic fields. In addition, the introduction of numerical phase detection has revealed the origin of the noise occurring in magnetic-field generation. We describe its mechanism and a reduction method in Sec. II B. Generally, the so-called "phase-rotation problem," which appears to rotate the phase as the frequency increases in AC measurements, cannot be neglected anymore. In Sec. II C, we discuss the method for dealing with this challenge. Finally, Sec. II D describes two methods to subtract specific backgrounds common to pulsed magnetic field experiments from the experimental data. For each technique described below, Table I shows the subsections in which the corresponding experimental results are described.

A. Numerical phase detection

In general, noise in DC measurements can be eliminated only by integrating data over a time much longer than the time scale of the noise, i.e., of the reciprocal of the noise frequency. If the time scale of the noise is longer than the integration time, it is difficult to remove it. We often encounter such a situation in transport measurements in pulsed magnetic fields because their measurement time scales are short, and many strong noise sources exist.

In this case, an effective noise-reduction method is the use of AC measurements. Among AC demodulation techniques, phase

TABLE I. Overview of the investigated experimental techniques and the subsections describing the corresponding experimental results.

Technique fundamentals	Expt. results
II A Numerical phase detection	
Numerical phase detection	III A
II B Noise origin and reduction	
Vibration of wires due to Lorentz force	III C$\langle 8 \rangle$
Mechanical vibration of probe	III A, III C$\langle 6 \rangle$
Differential vs single-ended signaling	III C$\langle 4 \rangle$
Choice of the modulation frequency	III C$\langle 2 \rangle$
Linear combination	III A, III C$\langle 3 \rangle$
II C Phase compensation	
Calibration of phase shift	III B
Asynchronization	III A, III C$\langle 5 \rangle$
II D Measurement background subtraction	
Phase inversion	III A
Magnetic flux compensation coil	III A, III C$\langle 7 \rangle$

detection is one of the most powerful methods. Generally, for the phase detection, when the angular frequency of the signal to be demodulated is ω_0 [see Eq. (A1) in Appendix A], we multiply the original signal by $2 \cos \omega_0 t$ [see Eq. (A2) in Appendix A] or $2 \sin \omega_0 t$ [see Eq. (A3) in Appendix A]. Then, we obtain mixtures of time-invariant components and second-harmonic oscillations. Next, we eliminate the components of the second-harmonic oscillation $\cos 2\omega_0 t$ and $\sin 2\omega_0 t$, whereby the time-independent components remain.

In actual pulsed-field measurements, roughly about 1000 data points are needed for a reasonable temporal resolution. This means that for tens of milliseconds long pulse duration, one data point should be acquired every tens of microseconds. Moreover, an AC analog demodulation method requires 100 up to 1000 oscillations per single data point. If we thus attempt to keep the aforementioned effective time resolution (i.e., tens of microseconds), the required modulation frequency will be in the order of several megahertz to several tens of megahertz. Since termination reflections become conspicuous in this frequency band, the impedance matching of the circuit is required, and conventional four-point measurements become challenging.

Contrary to analog AC demodulation, for the numerical phase detection method,[34] if the integral is performed in an interval of integer multiples of $2\pi/\omega_0$, the desired signal component can be extracted even within a small number (1, 2, 3, ...) of oscillation periods according to the relations of Eqs. (A4)–(A6) in Appendix A. For the above example, the necessary modulation frequency is about several tens of kilohertz. Since impedance matching of the circuit is not required in this frequency band, its associated circuit design becomes much easier. On the other hand, if the number of periods required to integrate the data is decreased, the noise reduction performance rapidly deteriorates because the pass gains G_n^{cc} and G_n^{cc}, which are defined in Eqs. (A7) and (A9) in Appendix A, remain relatively large at other frequencies than the modulation frequency. In

order to deal with this problem, several noise reduction techniques will be introduced, as discussed in Sec. II B.

B. Noise origin and reduction

Before considering the noise-reduction methods, we need to examine the cause of the noise inherent to pulsed magnetic fields. First, we need to examine how the setup performs in zero field. The goal now is to achieve a data quality in pulsed magnetic fields as close as possible to the zero-field performance.

The primary reason for the noise inherent to measurements in magnetic fields is that if wires are not sufficiently immobilized when an AC current flows through the signal line, the wires vibrate due to the Lorentz force. As a result, the effective area enclosed by the wire changes and an electromotive force is generated. Since the noise generated by such wire vibrations occurs in the same frequency range as the sample's modulation frequency, it is practically impossible to remove this noise using a numerical process. Therefore, in order to avoid such noise, it is necessary to fix the wire rigorously to the main body of the probe. This means that the construction of angular-rotation probes for low-noise measurements is challenging because such probes often require flexible wires.

Even after implementing such countermeasures, some noise remains, often at fixed, well-defined frequencies. The dominant source of residual noise is that the probe with a fixed wire loop experiences mechanical vibrations in an inhomogeneous magnetic field caused by the finite length of the magnet. Here, the frequency of the noise is the mechanical eigenfrequency of the probe or magnet.

Wiring manners of four-point resistance measurements are roughly categorized into the following two methods: (A) Only the core wires of four coaxial cables are used as signal lines and the outside of the coaxial cables are used as a shield, namely, the single-ended signaling method. (B) Both the core and shield of two coaxial cables or two twisted-pair cables are used as voltage and current lines, namely, the differential signaling method. We found that in pulsed magnetic fields, (B) has a better robustness against noise including the effect of leakage fields. For case (A), since the cross section surrounded by the wires is very large, the magnetic flux entering is large and electromotive forces can critically affect the signal quality.

By introducing a numerical phase detection, fast Fourier transformation (FFT) can be applied to the measured data at any time so that the noise spectrum can be easily disentangled. Moreover, if the noise spectrum is well reproducible, as in our case, it is easy to apply countermeasures.

The first measure is to separate the modulation frequency as far as possible from the noise frequency. Then, we use a first-order filter built from a capacitor and resistor (CR filter).

As mentioned before, in numerical phase detection, the noise-reduction performance deteriorates rapidly with a decreasing number of periods to integrate over the data. In this case, an additional noise-removal method is needed. Here, we discuss the noise-reduction methods detailed in Appendixes A–C.[35,36] Inherent noise components in pulsed magnetic fields often appear at specific frequencies, as mentioned above. On the other hand, in numerical phase detection, the pass gain varies depending on the number of periods to integrate over the data [see Figs. 1(a) and 1(d)], but the

zero point of the real part always coincides with the zero point of the imaginary part, even if a linear combination of pass gains is taken. By using this relation, it is possible to eliminate an arbitrary frequency independent of the modulation frequency.

For example, when we use a linear combination of the demodulated signal using one and two periods of the modulation frequency, it is possible to tune the frequency at which the pass gain becomes zero by changing the ratio of the coefficients [Figs. 1(c) and 1(d)]. Then, while keeping a good time resolution, it is possible to eliminate specific frequency components more efficiently than through the use of any analog filter.

When the number of periods used is further increased, the passing gains of multiple arbitrary frequencies can be set to 0 simultaneously (Appendix B 1). Furthermore, the order of such notch filters can be arbitrarily increased (Appendix B 3) and we can combine both filter techniques. Using these methods, theoretically, it is possible to transmit and receive data at a higher information density than the conventional OFDM (Orthogonal Frequency Duplicate Multiple) method that is currently widely used for wireless communication and broadcasting.

In this paper, we consider a high-pass filter that removes noise components sufficiently lower than the sample's modulation frequency (Appendix B 2). For example, in measurements performed in Yokohama (Sec. III A), the modulation frequency was 50 kHz and the noise frequency was around 5 kHz, which satisfies this condition well.

In this way, we can efficiently remove low-frequency noise components using data taken in a very short time using one and two modulation-frequency periods. In general, filters of various functions can be formed by taking linear combinations of demodulation results for various periods. This is a convenient way for noise removal through the inspection of the FFT spectrum of the signal after the measurement. This method can also be used for the high-speed removal of crosstalk in simultaneous measurements of multiple samples. For example, in measurements performed in Kashiwa (Sec. III C), the modulation frequencies of two samples were 20 kHz and 31.25 kHz, and their mixing frequency of 11.25 kHz was removed. The general principle and some applications of this method are described in the Appendixes A–C.

C. Phase compensation

Even though the modulation frequency can be drastically reduced by introducing numerical phase detection, a frequency of several tens of kilohertz is still higher than the frequency used for AC transport measurements in static magnetic fields. At such a high frequency, the phase shift between the input and output signals cannot be ignored. Here, we show a way to solve this issue.

In general, inserting a CR filter before the preamplifier essentially reduces the input impedance. This causes a voltage drop over the intermediate transmission line and results in a phase shift that is difficult to grasp. Therefore, the voltage line should be terminated by a preamplifier with a sufficiently large input impedance, and the CR filter should be placed after the preamplifier. We have calibrated the phase rotation angle and gain of the CR filter prior to any experiments accordingly: (1) Divide the output of the function generator into two separate signals, connect one directly to one channel of an oscilloscope, and let the other pass through the CR
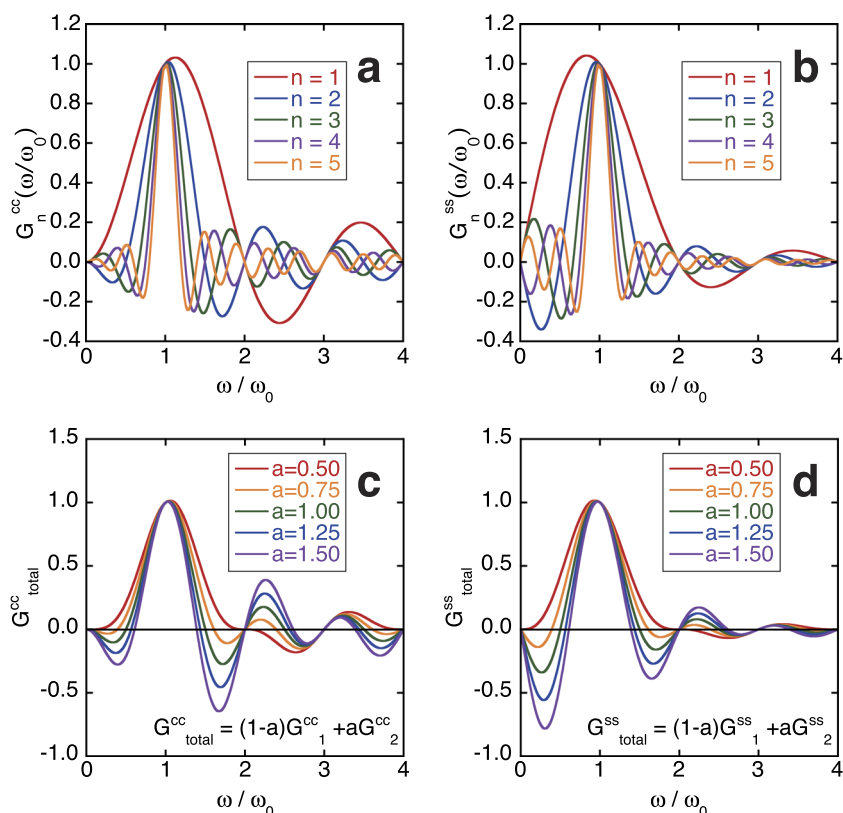
FIG. 1. (a) Real and (b) imaginary parts of the pass gain vs the normalized general angular frequency $x \equiv \omega/\omega_0$ for n periods of integration are shown. The pass gain strongly depends on n, except for $x = 1$. The zero positions of the real and imaginary parts coincide, as seen in Eq. (B2). In the range of $0 \leq x < 1$, generally, n zero points exist at equal intervals. (c) Real (G_{total}^{cc}) and (d) imaginary (G_{total}^{ss}) parts of the total pass gain of a linear combination of the results of phase detection for one and two period(s). Here, the pass gain of the signal frequency is normalized to unity. Whereas some zero points of the real and imaginary parts move depending on the weight of the coefficients, they appear always at the same ω. This fact strongly suggests that an arbitrary frequency component can be eliminated within a time resolution of 2 periods by tuning the weight of the coefficients.

filter and connect this signal to another channel of the oscilloscope. (2) Drive the function generator at the actual modulation frequency and record both signals simultaneously. (3) Demodulate both signals and extract the phase difference and amplitude ratio. In this way, we can reproduce the potential difference between the voltage terminals of the sample without rotating the phase. In the frequency band actually used, the influence of the stray capacitance between the lines is not crucial; however, it might be a point for future consideration.

Since the function generator and the oscilloscope have separate local oscillators, a phase shift may occur. In order to solve this problem, usually, we employ a synchronization technique in which one oscillator is used as a master and others are driven in slave mode. However, in the present case for the transient pulsed-field measurements, the rather slow synchronization feedback loop using a PLL VCO (Phase Locked Loop Voltage Controlled Oscillator) prevents such measures. Therefore, we simultaneously record the target and reference signal and apply our numerical phase detection to both. The reference signal in our transport measurements is obtained by placing a shunt resistor in series with the sample and reading the potential difference between the two ends of the shunt resistor by another channel of the oscilloscope. The TCXO [Temperature Controlled (X)crystal Oscillator] of the used devices has a frequency drift of several parts per million during the field pulse. Even after 1000 oscillation periods, the phase rotates by only a few degrees. For such small phase shifts, it is sufficient to calculate the phase shift,

from the measured real and imaginary parts of the reference signal using the arctangent function, and accordingly correct the phase of the target signal. Here, the error in the pass gain is smaller than a few parts per million, similar to the deviation of the frequency, so the error in the absolute value of the amplitude is negligible. Indeed, by dividing the target signal by the amplitude of the reference signal, we can correct for fluctuations of the reference signal, which further improves the accuracy of the measured signal. Since the arctangent function is a multivalued function, this often causes discontinuous jumps. As will be described later, it is possible to avoid the influence of this by using the function generator in burst mode, which provides a perfect reproduction of the phase.

D. Measurement background subtraction

Reproducible backgrounds, such as the induced electromotive force ($\propto dB/dt$) during magnetic field sweeps, are often not completely eliminated by integration over a short time. In such a case, it is quite effective to perform phase detection both with and without inverting the phase of the modulated wave and then take the difference between the two signals.

In order to support this procedure, the function generator should be used in burst mode driven by an external trigger. Moreover, the external trigger signal for the function generator must occur somewhat earlier than the trigger signal for the thyristor switch generating the pulsed magnetic field. As a result, reproducible

backgrounds are canceled and the combined amplitude of the signal components is doubled. This method can be realized because the reproducibility of the reference oscillation is much more precise than the tolerance (instrumental error of several parts per million) of the reference oscillation of the TCXO, as will be shown in Sec. III A for the data taken in Yokohama. Here, magnetic-field pulses could be generated frequently due to the short cooling time of the magnet. On the other hand, the pulse duration of the used magnet is short and the influence of dB/dt on the sample's signal is not negligible. For the measurements performed in Dresden and Kashiwa (see Secs. III B and III C), this technique was not adopted because the pulse duration was relatively long and the cooling time of the magnets was longer accordingly.

When the function generator is used in burst mode, the current flows through the sample for a very short time so that the Joule heating of the sample can be suppressed and the signal-to-noise ratio is improved.

The influence of the induced electromotive force ($\propto dB/dt$) on the signal's background can be reduced by adding a voltage proportional to the induced signal generated in a separate pick-up coil. This is a very effective way for removing this background in a situation where high-pass filters cannot be used. In particular, it has a great effect on the large dB/dt immediately after the start of the magnetic-field pulse. This allows us to reduce the dynamic range and improve the resolution by lowering the input range of the oscilloscope.

III. IMPLEMENTATION

In Sec. III A, specific examples of experiments in the three international magnetic field research facilities will be presented. In Yokohama, we devised a technique to remove noise components of a specific frequency efficiently by performing numerical processing. Moreover, the effectiveness of reducing the reproducible background by two measurements in which the phase of the applied current is inverted was confirmed. In Dresden, we established a compensation technique for phase rotation and verified its validity. In Kashiwa, we investigated the frequency dependence of the behavior of the real and imaginary parts of the signal under zero magnetic field and estimated its origin. The simultaneous measurements of two samples were also investigated to confirm any interference effects of the signals on each other. The experimental conditions used in each laboratory are shown in Tables II and III.

A. Yokohama

Here, we discuss a challenging experiment of measuring the magnetoresistance of a highly conductive metal in pulsed magnetic fields. As a result, we have succeeded to observe the Shubnikov–de Haas (SdH) oscillations in the nonmagnetic intermetallic compound LaB_4 as a reference material for the magnetic NdB_4 with Nd^{3+} ($4f^3$) forming a Shastry–Sutherland lattice.[37,38] This result shows that the numerical phase-detection method is appropriate for such measurements in pulsed magnetic fields.

1. Experimental

The transverse magnetoresistance of a single-crystalline sample of LaB_4 with a residual resistivity ratio (RRR) of 60 was measured for $I \parallel [100]$ and $B \parallel [010]$ at 4.2 K in magnetic fields up to 22 T.

The pulse duration was 15 ms and the energy was delivered by a 160 kJ capacitor bank. The sample was cut into the size of 1.87(0.72) $\times$ 0.94 $\times$ 0.98 mm^3. Here, the number inside the brackets indicates the distance between the voltage electrodes. At this point, as shown in Fig. 2(a), we used a single-ended input preamplifier (SA-200F3, NF Corp.). No high-pass but a self-made CR-type low-pass filter (cutoff frequency: 50 kHz, slope: 6 dB/oct) was used. The eddy-current effects had to be taken into account in the measurements. Therefore, we reduced this signal by using a compensation coil of inner diameter (i.d.) 3 mm $\times$ 3 turns, thereby reducing the dynamic range of the oscilloscope, thereby increasing the resolution. The background voltage remaining after the field compensation coil was canceled out by subtracting the result of a second measurement with inverting phase of the modulated wave. The sampling rate and vertical resolution of the recorder (DL750E, Yokogawa) are 1 MS/s and 16 bit, respectively. The modulation frequency was 50 kHz, so the number of data points for one modulation period was 20. The typical peak-to-peak amplitude of the applied current was 140 mA_{p-p}.

2. Results and discussion

Figures 2(b)–2(o) show the results for both excitations with positive and negative phases. The magnetic field [Fig. 2(e)], the current [Figs. 2(b) and 2(c)], and the voltage [Figs. 2(g) and 2(h)] are obtained by the induced electromotive force in a pickup coil, the potential difference across a shunt resistor, and the potential difference over the sample, respectively. In the overall envelope, no difference between the two data sets is observed. As seen in the detailed views (d), (j), and (k), the polarities of the signals are, indeed, inverted. The resulting difference signals of the current and voltage are shown in Figs. 2(f) and 2(i), respectively. Particularly, in the voltage signal, asymmetric components in the envelope, caused by the large dB/dt and other reproducible background signals, are successfully removed in the difference data [see Figs. 2(g)–2(i) and 2(j)–2(l), respectively]. We applied our numerical phase detection to both current and voltage signals. That is, both data were multiplied by $2 \cos \omega_0 t$ and $2 \sin \omega_0 t$ and a moving average (smoothing) of 20 points was applied. In this case, since the number of points is even, the trapezoidal rule for the numerical integration was applied. As can be seen in Fig. 3(b), the absolute value of the current is almost constant; however, both of the real and imaginary parts are varying, as shown in Fig. 3(a). Namely, the phase of the current is shifting due to the difference in the reference oscillation between the function generator and the oscilloscope. Dividing the real part of the current by the imaginary part and using the arctangent function, extract the time-dependent phase shift [see Fig. 3(c)]. In this experiment, the phase shifts by only 3.9° after 850 oscillations. For such small phase shifts, the phase can be corrected numerically [see Figs. 3(d) and 3(e)]. Finally, the voltage divided by the current gives the resistance. In this experiment, a filter was placed in front of the preamplifier and the phase rotation due to the impedance of the filter was not corrected. This was done in the later experiments in Dresden. Therefore, some uncertainty in the phase correction remains. We tuned the phase so that the magnetic quantum oscillations appear mainly in the real part of the resistance [Fig. 3(f)]. When plotting the resistance as a function of magnetic field [Fig. 4(a)], the oscillations for rising and falling fields coincide very well. This shows the high quality of the data acquisition.

TABLE II. The measurement conditions in each experiment in Yokohama and Dresden.

	Yokohama	Dresden
Sample	LaB_4	$PrIr_2Zn_{20}$
Size: length × width × thickness[a]	$1.87(0.72) \times 0.94 \times 0.98$ mm^3	$2.8(1.55) \times 0.492 \times 0.276$ mm^3
Current (I) direction	$\parallel [1\bar{1}0]$	$\parallel [1\bar{1}0]$
Field (B) direction	$\parallel [111]$	$\parallel [111]$
Magnetic fields		
Peak fields[b] (T)	22	61
Duration time (ms)	15	300
Max. energy	160 kJ	50 MJ
Temperature (K)	4.2	1.6–20
Instruments		
Function generator	1/2 WF1966 (NF corp.)	DS360 (Stanford)
Modulation frequency (kHz)	50	16.6667
Typical current	140 mA$_{\text{p-p}}$	50 mA$_{\text{p-p}}$
Periods in burst mode	850	5000
First preamplifier	SA-200F3 (NF Corp.)	SA-400F3 (NF Corp.)
Gain	100	100
Second preamplifier	Null	Null
	. . .	. . .
Gain	. . .	. . .
Oscilloscope	DL750E (Yokogawa)	DL850E (Yokogawa)
Sampling rate (MS/s)	1	1
Vertical resolution	16 bit	16 bit
Number of data points	20 000	200 000
Analog filter	Handmade	In DL850E
LPF	50 kHz	40 kHz
Slope	6 dB/oct	6 dB/oct
HPF	Null	Null
Slope	. . .	. . .
Magnetic flux compensation coil		
Inner diameter (mm)	3	3
Number of turns	3	3
Time resolution (μs)	40	120
Data points per one period	20	60
Periods for demodulation	1 and 2	1 and 2

[a]The number inside the brackets indicates the distance between the voltage electrodes.
[b]These values are not the maximum possible magnetic fields of these systems but the maximum magnetic fields generated for our experiments.

When performing an FFT of the background subtracted resistance ΔR as a function of $1/B$, multiple SdH frequencies can be resolved [Fig. 4(b)]. This shows that with our method, we are able to resolve SdH oscillations in metallic samples having a resistance of only a few microhms.

In the FFT of the raw voltage data, shown in Figs. 2(g) and 2(h), a peak around 5 kHz is observed, as shown in Figs. 2(m) and 2(n). Although this frequency hardly changes between the two measurements, a small peak remains in the difference signal [Fig. 2(o)]. Therefore, the reproducibility of the phase and amplitude is not

TABLE III. The measurement conditions in each experiment in Kashiwa.

	Measurement I		Measurement II	Measurement III
	Channel 1	Channel 2		
Sample	Au wire "Sample A"	Ag wire "Sample B"	Pt wire	Cu–Ag wire
Size: diameter × length[a]	0.05 mm × 3.5(0.3) mm	0.05 mm × 3.5(0.3) mm	0.05 mm × 3.5(0.3) mm	0.05 mm × 3.5(0.3) mm
Current (I) direction	$\perp B$	$\perp B$	$\perp B$	$\perp B$
Field (B) direction	$\perp I$	$\perp I$	$\perp I$	$\perp I$
Magnetic fields				
Peak fields[b] (T)	31		11	33
Duration time (ms)	11		11	37
Max. energy (kJ)	600		600	900
Temperature (K)	4.2, 78		78	4.2
Instruments				
Function generator	1/2 WF1966 (NF Corp.)	2/2 WF1966 (NF Corp.)	1/2 WF1966 (NF Corp.)	1/2 WF1966 (NF Corp.)
Modulation frequency (kHz)	1–62.5	1–62.5	25	10
Typical current	190 mA$_{\text{p-p}}$	0 or 190 mA$_{\text{p-p}}$	190 mA$_{\text{p-p}}$	190 mA$_{\text{p-p}}$
Periods in burst mode	40–2500	40–2500	375	440
First preamplifier	SA-410F3 (NF Corp.)	SA-410F3 (NF Corp.)	SA-410F3 (NF Corp.)	SA-410F3 (NF Corp.)
Gain	100	100	100	100
Second preamplifier	SR560 (Stanford)	SR560 (Stanford)	SR560 (Stanford)	SR560 (Stanford)
Gain	1	1	1	1
Oscilloscope	DL850E (Yokogawa)	DL850E (Yokogawa)	DL850E (Yokogawa)	DL850E (Yokogawa)
Sampling rate (MS/s)	1	1	1	1
Vertical resolution	16 bit	16 bit	16 bit	16 bit
Number of data points	20 000	20 000	20 000	50 000
Analog filter	BPF in SR560	BPF in SR560	BPF in SR560	BPF in SR560
LPF	...	...	100 kHz	30 kHz
Slope	6 dB/oct	6 dB/oct	6 dB/oct	6 dB/oct
HPF	...	...	10 kHz	3 kHz
Slope	6 dB/oct	6 dB/oct	6 dB/oct	6 dB/oct
Magnetic flux	Null	Null		Null
Compensation coil				
Inner diameter	...	...	2 mm	...
Number of turns	...	...	57	...
Time resolution	16 μs–1 ms	16 μs–1 ms	100 μs	40 μs
Data points per one period	16–1000	16–1000	40	100
Periods for demodulation	1–3	1–3	1 and 2	1 and 2

[a]The number inside the brackets indicates the distance between the voltage electrodes.
[b]These values are not the maximum possible magnetic fields of these systems but the maximum magnetic fields generated for our experiments.

perfect. We assume that the 5 kHz frequency is caused by the mechanical eigenfrequency of the probe.

In the following, we show how to increase the signal-to-noise ratio according to the method described in Sec. II B. Figures 5(a) and 5(b) show the R vs B curves for the case where the integration interval is taken over one (20 points) and two periods (40 points) of the modulation, respectively. Although, overall, the two curves

seem to be identical, they differ in details. This mismatch is due to the fact that the pass gain for frequencies except for the modulation frequency differs for the integration interval over one and two periods. According to the above theory, we take the sum of both and divide by two. By that, the sharp peaks and valleys are canceled out and become smooth, as shown in Fig. 5(c). The time resolution of this method is the same as that for the demodulation using two
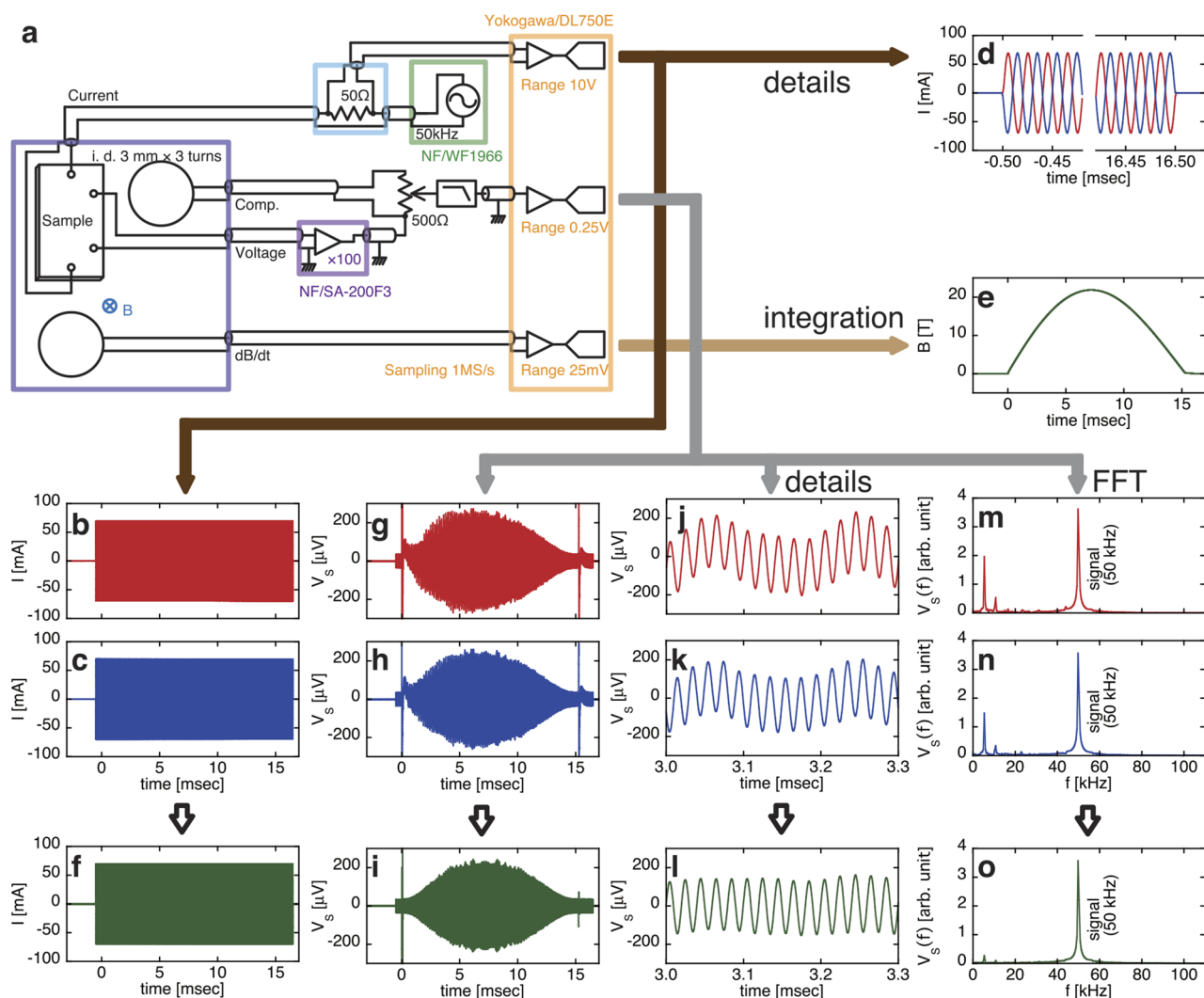
FIG. 2. Diagram of the circuit and raw data of magnetoresistance measurements of LaB_4. (a) The diagram of the circuit used to measure the transverse magnetoresistance of LaB_4 in Yokohama. A single-ended preamplifier was used at that time. Instead of a high-pass filter, a dB/dt compensation coil was used. A handmade low-pass filter was employed. Time dependence of the applied current with (b) normal and (c) reversed phase. (d) shows the details near the start and end point of the applied current, respectively. (e) Highly reproducible time dependence of the pulsed magnetic field. Therefore, the additional phase shift between the two measurements is very small, as seen in (d). Thus, we may perform phase detection on (f), which is the measurement result using the normal phase minus the result with reversed phase. This makes it possible to subtract nicely the reproducible background. The actual normal and reversed phase output voltages and the difference between them are shown in (g)–(i), respectively. The asymmetry in (g) and (h) (i.e., the background considered to be due to dB/dt) disappears in (i). Furthermore, it can be seen that an oscillatory signal of about 5 kHz is considerably suppressed, according to the detailed views (j)–(l) corresponding to (g)–(i). This fact is also evident in the FFT spectra (m)–(o) of these signals. This subtraction is, however, not perfect. The remainder can be removed by using another technique described below (Fig. 5).

periods, but the noise removal performance is far superior. Whereas a numerical high-pass filter was chosen in this example, in general, after acquiring the data, it is possible to analyze the frequency component of the noise and perform optimum processing on the data. Unlike analog filters, these methods do not cause phase rotation of the signal. This method also has the great advantage that noise can be eliminated after the measurements.

Finally, we have realized an extremely high resistance resolution of several 10 $\mu\Omega$ within a time window of at most 40 μs in

the present experiment. From the dimensions of this sample, the resolution in terms of resistivity is estimated to be several $\mu\Omega$ cm.

B. Dresden

$PrIr_2Zn_{20}$ is a cubic-lattice superconductor in which the Pr^{3+} ion has a nonmagnetic non-Kramers Γ_3 doublet ground state. Therefore, it has been frequently discussed whether in this material, quadrupolar interactions mediate Cooper-pair coupling.[39,40] Here,
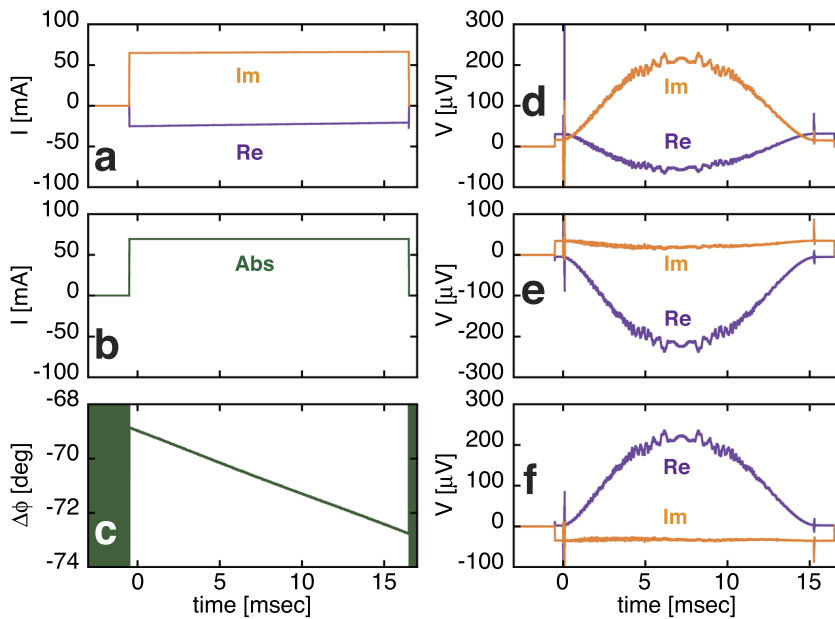
FIG. 3. (a) Real and imaginary parts of the current values phase-detected from the data shown in Fig. 2(c). (b) Absolute value and (c) phase shift of the current obtained. (d) Real and imaginary parts of the voltage phase-detected from the data shown in Fig. 2(i). (e) Real and imaginary parts of the voltage based on the phase of the current. (f) Orthogonal transformation of (e), which maximizes the signal's time-dependent changes in the real part and keeps the imaginary part constant.

we report on the observation of SdH oscillations in this material. In general, the extremal-area cross section of the Fermi surface can be obtained by analyzing the frequency of this oscillation.

1. Experimental

Here, the transverse magnetoresistance of a single-crystalline sample [2.80(1.55) × 0.429 × 0.276 mm^3] was measured in magnetic fields up to 61 T at 1.6 K, 4.2 K, 6.5 K, 10 K, and 20 K for $I \parallel [1\bar{1}0]$ and $B \parallel [111]$. The magnetic-field pulse duration was about 150 ms. The necessary energy of about 8 MJ was supplied by a 50 MJ

capacitor bank. A differential-type preamplifier (SA-400F3, NF Corp.) was used. A typical current of 40 mA$_{p-p}$ with a modulation frequency of 16.6667 kHz was applied by a function generator (DS360, Stanford Research Systems). 60 data points were recorded per modulation-frequency period using a digital-storage oscilloscope [DL850E (16 bits, 1 MS/s), Yokogawa]. A built-in low-pass filter with a cut-off frequency of 40 kHz and a slope of 6 dB/oct in the oscilloscope was used. Moreover, a dB/dt compensation coil of i.d. 3 mm × 3 turns was used after the preamplifier to remove the dB/dt component (see Fig. 6). Since the cooling time of the used magnet after each field pulse is about 2 h, no measurements with inverted
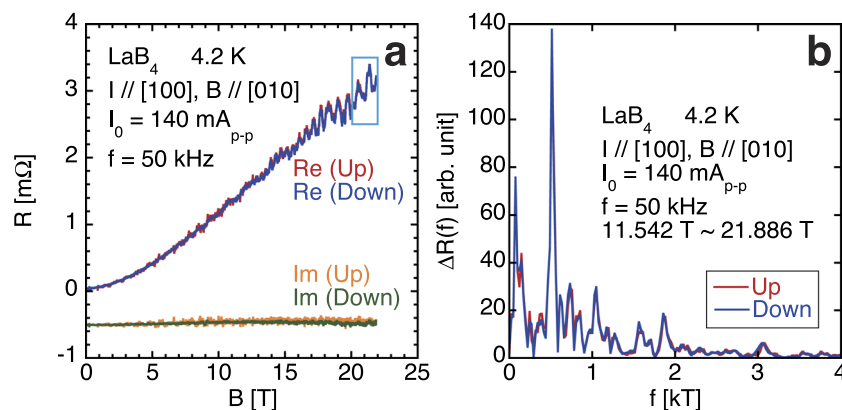
FIG. 4. (a) Resultant field-dependent magnetoresistance of LaB$_4$. The data for rising and falling fields are shown in red and blue for the real part, respectively, and in orange and green for the imaginary part, respectively. Prominent SdH oscillations appear at high magnetic fields, without any noticeable hysteresis for up and down sweep. The data in the light blue rectangle are shown in Fig. 5 in an enlarged scale. (b) Fast Fourier transformed ΔR as a function of $1/B$. Here, a fourth-order polynomial fit to the real part of the magnetoresistance (a) was used to determine ΔR. The results for the up and down sweep are shown in red and blue, respectively. Both results agree well with each other.
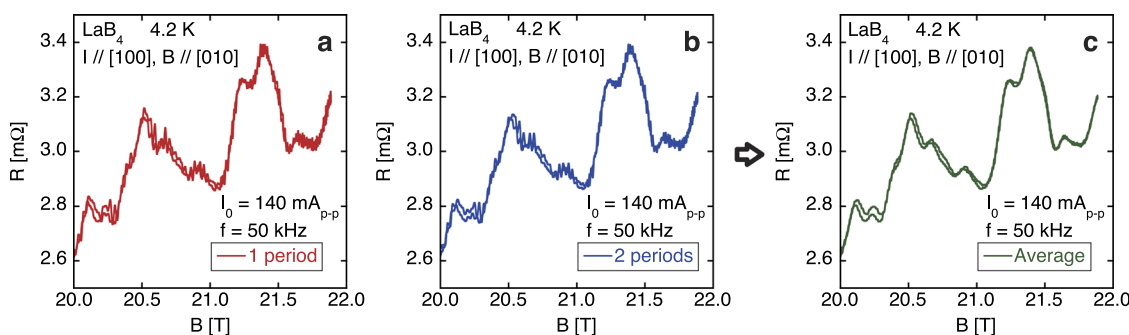
FIG. 5. Enlarged view of the high-field data of LaB$_4$ shown in Fig. 4(a). (a) Results after demodulation using one modulation-frequency period and (b) after using two periods. (c) Average of both results. While the data in (c) have the same time resolution as those shown in (b), the noise rejection is drastically higher in (c). This principle corresponds to the case of $m = 2$ discussed in Sec. B 2 of Appendix B.

current were performed. We performed, however, the same signal processing as in Fig. 5, i.e., averaging the results of one and two modulation periods. This operation is equivalent to a high-pass filter. Therefore, it is considered to be effective in suppressing the influence of dB/dt, which is a frequency component sufficiently lower than the modulation frequency, although it is not as effective as the phase-inverting method.

2. Results and discussion

The phase-shift compensation due to reference-oscillator differences between the function generator and the oscilloscope was carried out as discussed before for the Yokohama experiments in Sec. III A. Here, we will explain a method for canceling the phase shift due to other effects. The relatively long signal lines were terminated by a preamplifier with a relatively large input impedance of 100 kΩ. The resulting voltage drop due to the self-inductance and the resistance of the intermediate wires could, thus, be substantially

eliminated, and a possible phase rotation in this part of the circuit was prevented.

The rotation of the phase caused by the filter, the preamplifier, and the compensation coil was experimentally determined. Thereby, the modulation signal from the function generator was connected directly to one channel of the oscilloscope as well as to one of the mentioned devices. The output from the devices was then connected to a second oscilloscope channel (Fig. 7). We have determined 32.30° as the total phase shift due to the measurement circuit by this calibration.

Based on this calibration, we separated the result of the magnetoresistance measurement at 1.6 K into its real and imaginary parts, as shown in Fig. 8.

In the real part, on a monotonously increasing background, we find clear and reproducible oscillations as a function of magnetic field [Fig. 9(a)]. With increasing temperature, the oscillations occur at the same magnetic fields but decrease in amplitude.
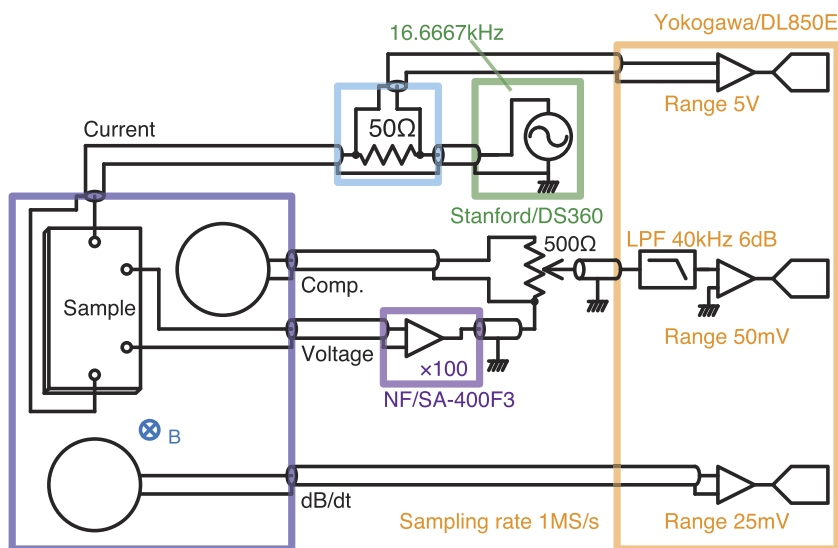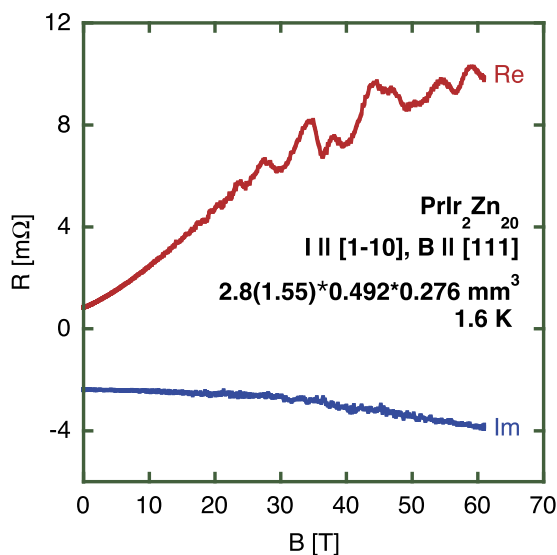

FIG. 6. Diagram of the circuit used to measure the transverse magnetoresistance of PrIr$_2$Zn$_{20}$ in Dresden. Instead of a high-pass filter, a dB/dt compensation coil was used. A built-in low-pass filter of the oscilloscope was employed.
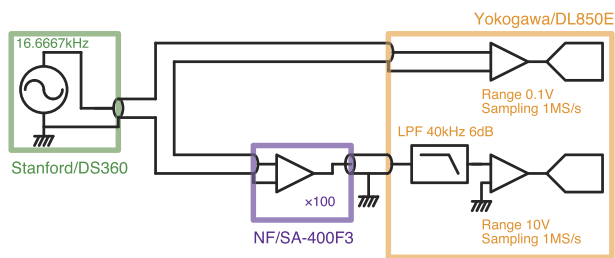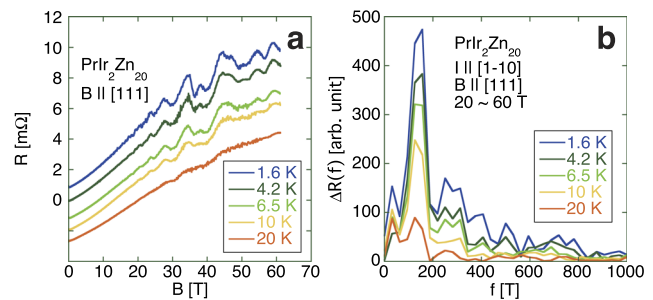
FIG. 7. Method to determine the output phase shift and the gain of devices used in the circuit of Fig. 6. The output phase shift and gain of the device are calibrated by a comparison of the phase difference and amplitude ratio with respect to a direct signal from the function generator.

FIG. 9. (a) Transverse magnetoresistance vs magnetic field measured during down sweeps of PrIr$_2$Zn$_{20}$ at 1.6 K, 4.2 K, 6.5 K, 10 K, and 20 K. The data are vertically offset for clarity. At high magnetic fields, clear SdH oscillations are visible, which decrease in amplitudes with increasing temperature. (b) Temperature dependence of the FFT of the background-subtracted magnetoresistance vs 1/B. The background was approximated by a fourth-order polynomial.

Several peaks appear in the FFT of the background-subtracted data as a function of 1/B [Fig. 9(b)] evidencing the SdH-effect nature of the observed oscillations. This reflects the high resolution of our pulsed-field experiment on a microhm sample. An in-depth scientific discussion of these results is beyond the scope of this technical/instrumental paper and will be provided in a separate publication. In the imaginary part of the signal (Fig. 8), no SdH oscillations can be resolved. The monotonous decrease of this signal with field indicates that the orthogonal axes of the real and imaginary parts are properly chosen. Then, the imaginary part is affected by parasitic mutual inductances near the sample, i.e., the current and voltage lines around the sample behave as primary and secondary coils of a transformer, respectively. As this only affects the imaginary part of the signal, an unambiguous separation from the real part can be carried out, also separating the influence of the phase rotation, yielding a reliable absolute value of the signal.
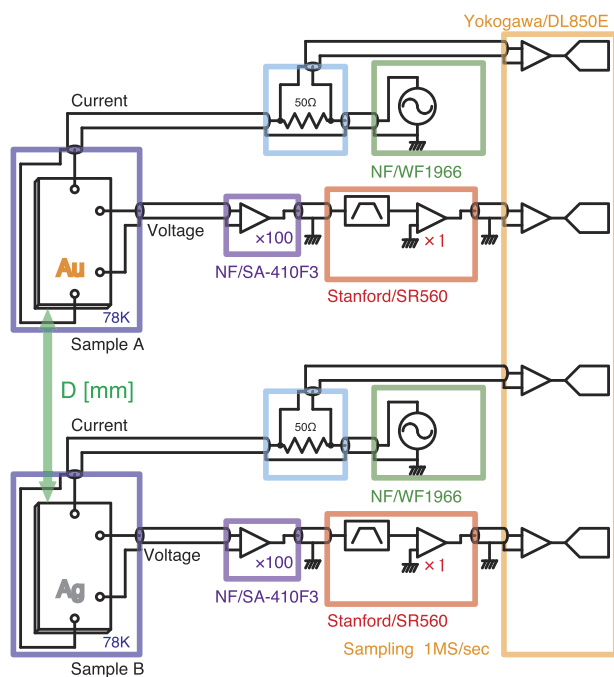
C. Kashiwa

In Sec. III B, it has been confirmed that the real and imaginary parts of the signal can be separated without any arbitrariness by calibrating the gain and phase shift of the amplifier and the filter. Here, we will further examine the frequency dependence of the real and imaginary signal parts. We will also describe the signal interference due to the simultaneous measurement of two samples. In addition, we examine the remaining topics listed in Table I.

1. Experimental

a. Measurement I. Gold (sample A) (99.95% TANAKA Kikinzoku Kogyo K.K.) and silver (sample B) (99.95% TANAKA Kikinzoku Kogyo K.K.) wires with a diameter of 0.05 mm were prepared as test samples. The used function generator WF1966 (NF Corp.) has two output channels. Channel 1 was connected to sample A and channel 2 was connected to sample B. We prepared two independent circuits with the preamplifier SA-410F3 (NF Corp.) as the first stage and the preamplifier SR560 (Stanford Research Systems) as the second stage (see Fig. 10). We performed five experiments under the following conditions:

1. An AC current of the same amplitude but with various frequencies (1 kHz, 2 kHz, 3.125 kHz, 4 kHz, 5 kHz, 6.25 kHz, 10 kHz, 20 kHz, 31.25 kHz, 40 kHz, 50 kHz, and 62.5 kHz) was applied to sample A during 40 ms, but no current was applied to sample B. The filter built into the latter amplifier was set to flat (DC) mode. The gain and phase shift of the amplifiers at each frequency were calibrated according to the concept described in Sec. III B. Another gold wire having a diameter of 0.02 mm was used for the current and voltage leads. The two samples with their leads were fixed ~15 mm apart from each other on the same probe with GE varnish.

2. Using the circuit depicted in the top half of Fig. 10, the magnetoresistance of the gold wire was measured at 10 kHz (6 dB/oct BPF: 3–30 kHz) and 25 kHz (6 dB/oct BPF: 10–100 kHz) at 4.2 K in fields up to 31 T in order to investigate any frequency dependence. Each of the sample's current and voltage leads was soldered to a terminal on individual printed circuit boards. The

FIG. 8. Real (red line) and imaginary (blue line) parts of the experimentally obtained resistance of PrIr$_2$Zn$_{20}$ as a function of magnetic field.

FIG. 10. Circuit diagram for *Measurement I* ⟨1⟩–⟨3⟩. The resistance of two samples (gold wire and silver wire) is measured simultaneously. Bandpass filters are employed instead of a compensation coil for canceling the *dB/dt* component. The frequencies, current amplitudes, and filters are set individually. D is the distance between both samples, which is about 15 mm in ⟨1⟩ and 5 mm in ⟨3⟩, respectively.

two samples were fixed ~5 mm apart from each other on the same probe with GE varnish.

3. We measured the magnetoresistance of both samples A and B individually as well as simultaneously at 4.2 K in fields up to 11 T with a pulse duration time of 11 ms. In both cases, AC currents with frequencies of 20 kHz and 31.25 kHz and peak-to-peak amplitudes of 190 mA were applied to samples A and B individually, respectively.

4. We tested whether differential signaling outperforms single-ended signaling.

5. We surveyed the synchronization of the oscilloscope's and function generator's crystal oscillators experimentally through the analysis of the phase shift of a 25 kHz signal.

6. Using a glass Dewar with an inner diameter of 10 mm and an fiber-reinforced-plastic (FRP) probe with an outer diameter of 6 mm, we compared three specific mechanical noise-reduction methods. (A) The Teflon tape is wrapped around the tip of the probe so that it tightly fits inside the Dewar. (B) A SUS304 pipe with an outer diameter of 8 mm, a wall thickness of 0.5 mm, and a length of 61 mm is attached to the tip of the probe. (C) Nothing is attached to the tip of the probe.

b. Measurement II.

7. In order to investigate the effect of a compensation coil, we measured the magnetoresistance with [Fig. 21(f)] and without [Fig. 21(a)] a magnetic flux compensation coil in fields up to

11 T with a pulse duration of 11 ms. Here, the magnetic pulse waveform is shown in Fig. 20(a). The sample was a platinum wire (99.98%, The Nilaco Corporation) with an outer diameter of 0.05 mm, and we also prepared a compensation coil with an outer diameter of 2 mm and 57 turns. The sample's current and voltage leads were soldered to four terminals on individual printed circuit boards and fixed on a probe with GE varnish. We performed measurements with and without a bandpass filter in both of the measuring circuits.

c. Measurement III.

8. A copper-silver-alloy (6 wt. % of Ag) filament with a rectangular cross section (~0.05 mm × ~0.05 mm) was prepared as a test sample. A gold wire having a diameter of 0.02 mm was used for the current and voltage leads. In order to investigate the effect of wiring vibrations due to the Lorentz force, we measured the magnetoresistance of the filament at 78 K in fields up to 33 T with a pulse duration of 37 ms, as shown in Fig. 22(c).

2. Results and discussion

a. Measurement I.

1. The results are shown in Fig. 11. The measured voltage signal of sample B [Fig. 11(b)] shows a dominant imaginary component, which is linear in frequency, but a real component that is very small. This indicates that the main cause of crosstalk is due to the mutual inductance between the wirings.

   Figure 11(a) displays the measured voltage over sample A. Here, the real signal component is finite and almost independent of frequency and the imaginary component decreases linearly with frequency. This strongly suggests that the former is derived from the actual resistance of the sample and the latter is caused by the mutual inductance between the current and voltage leads of sample A, similar to the crosstalk observed in sample B. From the fact that the imaginary component of the signal is small and the real component only displays a minute frequency dependence, we conclude that the separation of the real and imaginary components has been performed correctly.
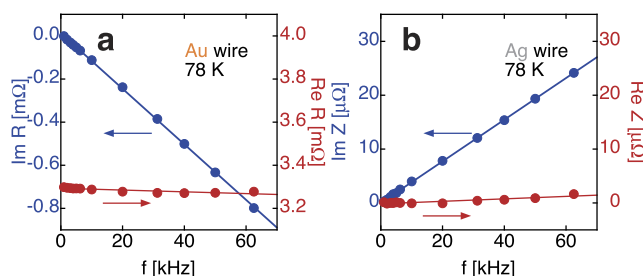
FIG. 11. Frequency dependence of the potential difference between the voltage terminals of the (a) Au and (b) Ag wire, respectively, with the current flowing in the Au wire at 78 K. The imaginary part in (a) decreases and in (b) increases linearly with frequency. On the other hand, the frequency dependence of the real part is much smaller than that of the imaginary part. Particularly, the real part in (b) is almost negligible.

This is consistent with the experimental results in Sec. III B, where the SdH signal appears in the measured signal's real part but not in the imaginary part.
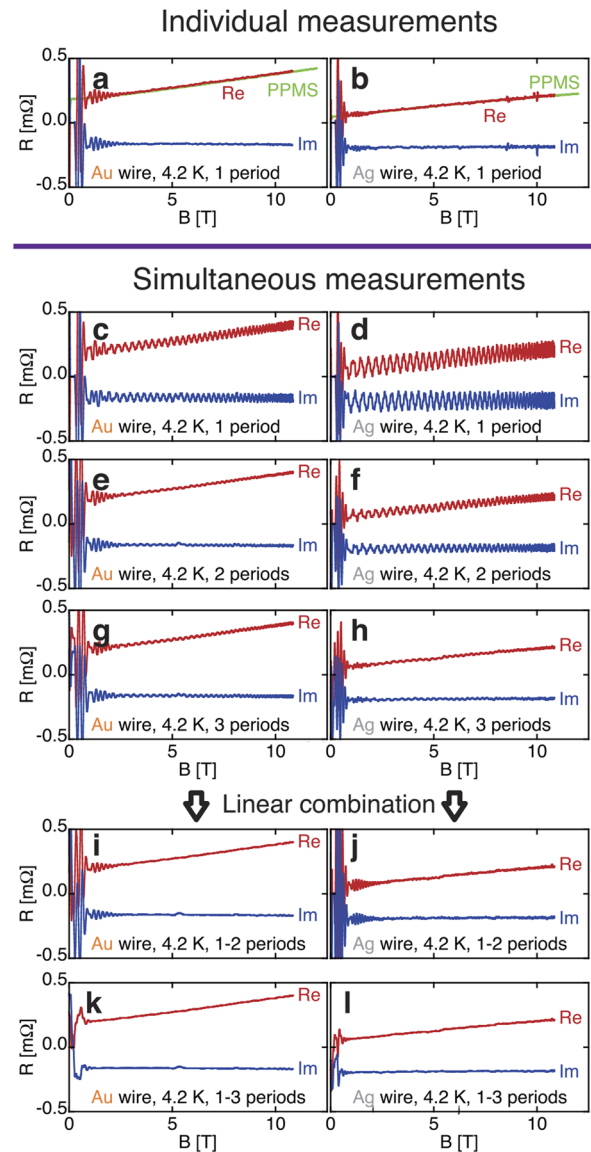
2. We measured the magnetoresistance of a gold wire at frequencies of 10 kHz and 25 kHz up to 31 T at 4.2 K. Here, the phase and gain of the preamplifier and filter were calibrated for each frequency by the method described in Sec. III B. As shown in Fig. 12(a), the real parts for both frequencies match very well with each other. On the other hand, the imaginary parts are frequency- and magnetic-field dependent, but their magnitudes seem to be roughly proportional to the frequency.

These experimental results evidently show that the real part is the actual magnetoresistance of the sample and the imaginary part is due to the influence of the mutual inductance of the wiring around the sample, and prove that our method can correctly separate the real and imaginary parts. The details of the magnetoresistance results using one modulation-frequency period and corresponding FFT spectra of the voltage are shown in Figs. 12(b) and 12(c), respectively. The oscillation on the magnetoresistance data is dominantly due to the components of dB/dt with 45 Hz, as will be explained in more detail in the following paragraph ⟨3⟩ as well as in *Measurement II* ⟨7⟩. We can suppress this vibration by looking at the FFT results and making a decision to move the modulation frequency away from DC. That is, in this case, it can be predicted in advance that a result with a lower oscillation amplitude can be obtained at 25 kHz than at 10 kHz.

3. First, the magnetoresistance of the Au and Ag wire was measured individually at 20 kHz and 31.25 kHz, respectively. Using one demodulation period, the results for the Au and Ag wires are shown in Figs. 13(a) and 13(b), respectively. The results
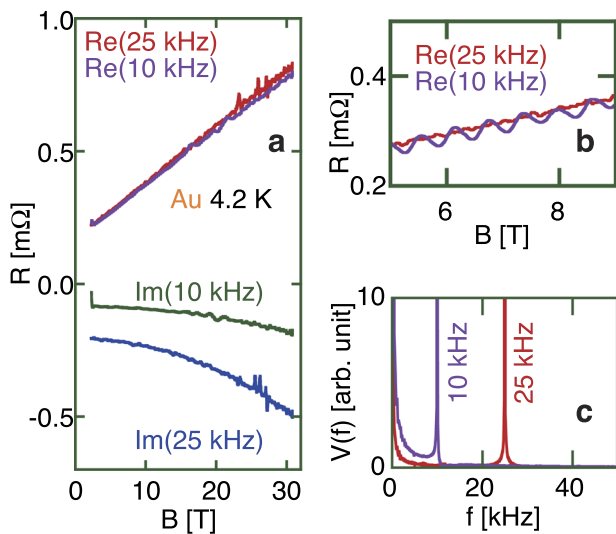
FIG. 12. (a) Magnetoresistance of the gold wire at 4.2 K for signal frequencies of 10 kHz and 25 kHz using appropriate bandpass filters. The data are only shown for the down sweep of the 31 T pulse. Here, the signals were averaged, as shown in Fig. 5(c). (b) The details of (a) demodulated using one modulation-frequency period. (c) FFT spectra of the voltage signals in a linear scale for signal frequencies of 10 kHz and 25 kHz.

FIG. 13. Results of individual measurements of the magnetoresistance of (a) Au and (b) Ag wires. Demodulated results of the simultaneous measurement of the magnetoresistance of both wires by using data of (c) and (d) one, (e) and (f) two, and (g) and (h) three modulation-frequency periods for the Au and Ag sample, respectively. (i) [(j)] Linear combination of the data of (c) and (e) [(d) and (f)], weighted to cancel the crosstalk. (k) [(l)] Linear combination of the data of (c), (e), and (g) [(d), (f), and (h)], weighted to cancel not only the crosstalk but also the lower-frequency background. The red and blue lines show the real and imaginary parts of the measurement results in pulsed magnetic fields, respectively. The green lines in (a) and (b) show the measurement results in quasi-static magnetic fields by using a PPMS (Physical Property Measurement System/Quantum Design, Inc.).

in quasi-static magnetic fields up to 12 T by using a PPMS are also shown in Figs. 13(a) and 13(b) as green lines. For both samples, this visualizes the high consistency between the results obtained in pulsed magnetic fields with those in

quasi-static-magnetic fields. Next, their magnetoresistance was measured simultaneously. Similarly, the results of the demodulation using one, two, and three periods are displayed in Figs. 13(c), 13(e), and 13(g) for the Au wire and Figs. 13(d), 13(f), and 13(h) for the Ag wire, respectively. The results clearly show that oscillatory components are superimposed on the results. The FFT spectra indicate large frequency components of 31.25 kHz and 20 kHz in addition to the modulation frequencies of 20 kHz and 31.25 kHz in Figs. 14(a) and 14(b), respectively. This means that the modulation frequency of the respective other sample is superimposed on the signal of interest. FFT spectra of the resulting resistance of Figs. 13(c)–13(h) are shown in Figs. 15(a)–15(f), respectively. Figures 15(a), 15(c), 15(e) [Figs. 15(b), 15(d), 15(f)] corresponding to the Au (Ag) wire show the frequency components 11.25 kHz (11.25 kHz) and 20 kHz (31.25 kHz) in addition to the DC component. The former is the crosstalk effect from the other sample as mentioned above, but the latter is considered to be due to dB/dt of ≈ 45 Hz, which is a very low frequency compared to the modulation frequencies of 20 kHz and 31.25 kHz. Figures 16(a)–16(d) show the simulation results of the passing gains G_n^{cc} and G_n^{ss} defined in Eqs. (A7) and (A9) of Appendix A associated with these demodulation processes. Here, n is defined as the number of periods. G_n^{cc} and G_n^{ss} of the Au (Ag) wires are nonzero at 11.25 kHz (11.25 kHz) and 20 kHz (31.25 kHz) for $n = 1$, 2, and 3. It can be easily understood that simply increasing the number of integration periods does not eliminate these oscillation components easily. Here, we attempt to remove these unwanted frequency components by using their passing-gain difference due to the difference in modulation periods, as shown in Appendix B 1.

First, consider the case of $m = 2$ in Eq. (B5) of Appendix B 1 to cancel the counterpart-frequency component. The equation to be solved is as follows:

$$\begin{pmatrix} 1 & 1 \\ G_1^{ss}(x_1) & G_2^{ss}(x_1) \end{pmatrix} \begin{pmatrix} a_1 \\ a_2 \end{pmatrix} = \begin{pmatrix} 1 \\ 0 \end{pmatrix}. \quad (1)$$
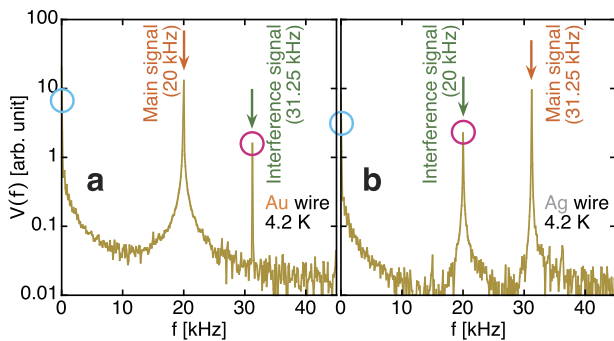

FIG. 14. (a)–(j) FFT spectra of the magnetoresistance in a logarithmic scale of the Au and the Ag wire in simultaneous measurements. The corresponding resulting magnetoresistance is shown in Figs. 13(c)–13(l), respectively. The cyan and magenta circles indicate the positions of the modulation and crosstalk frequencies, respectively.
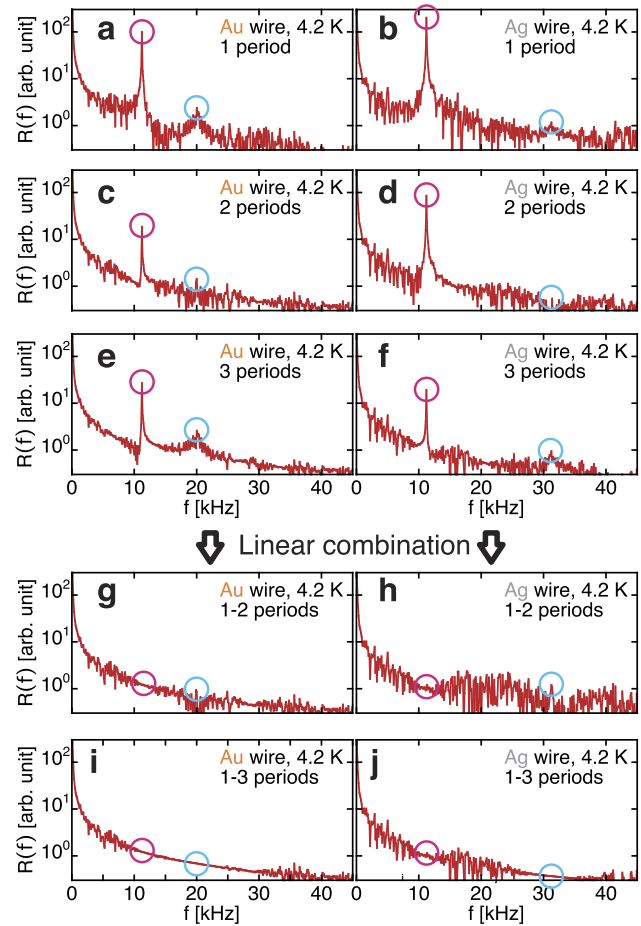
FIG. 15. FFT spectra of the magnetoresistance in a logarithmic scale of the Au and the Ag wire in simultaneous measurements. The corresponding resulting magnetoresistance is shown in Figs. 13(c)–13(l). The cyan and magenta circles indicate the positions of the modulation and crosstalk frequencies, respectively.

Here, 31.25/20 (20/31.25) is chosen as x_1 for sample A (B), and then we obtain $a_1 = 0.163$ (-0.741) and $a_2 = 0.837$ (1.741), respectively. Figures 13(i) and 13(j) show the results of the weighted sum of the data obtained by analyzing one and two periods, with the corresponding FFTs shown in Figs. 15(i) and 15(j). It can be seen that the frequency component of 11.25 kHz is significantly reduced compared to the data before the linear combination. The corresponding passing gains G_{total}^{cc} and G_{total}^{ss} defined in Eqs. (A12) and (A11) of Appendix A are used for the Au (Ag) wire measurements for the case of $m = 2$ in Figs. 16(e) and 16(f) [Figs. 16(g) and 16(h)], respectively. The values of G_{total}^{cc} and G_{total}^{cc} for $m = 2$ are clearly 1 and 0 at 20 kHz and 31.25 kHz (31.25 kHz and 20 kHz) for the Au (Ag) wire measurements, respectively. In Figs. 13(i) and 13(j), the oscillations in the high-field region have disappeared accordingly. However, oscillations in the low-field region still remain. The oscillations are due to dB/dt, which corresponds to the low frequency and needs to addition of a high-pass filter (HPF) for further suppression.
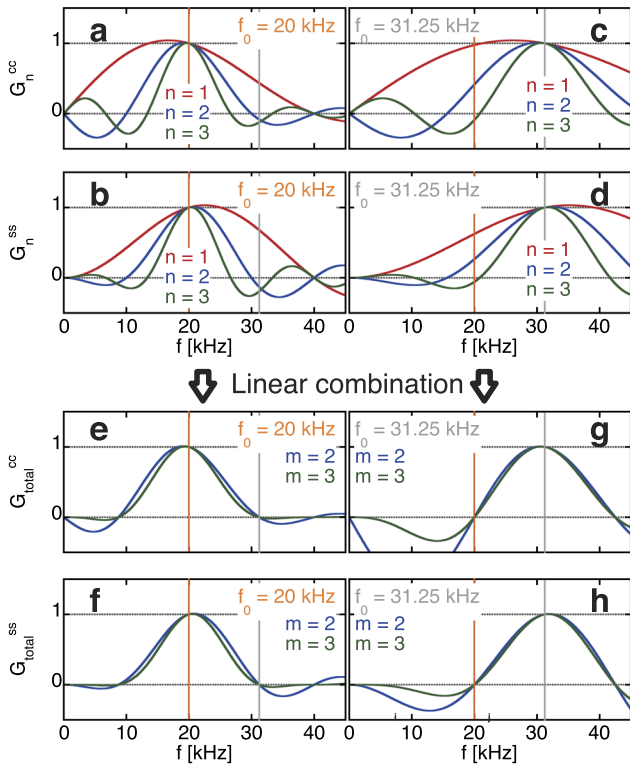
FIG. 16. Simulation results of the pass gain of the numerical phase detection for modulation frequencies of 20 kHz and 31.25 kHz. (a) G_n^{cc} in Eq. (A7) and (b) G_n^{ss} in Eq. (A9) for the 20 kHz signal using one ($n = 1$), two ($n = 2$), and three ($n = 3$) modulation-frequency periods. (c) G_n^{cc} and (d) G_n^{ss} for the 31.25 kHz signal using one, two, and three modulation-frequency periods. (e)/(g) Linear combination of the data for $n = 1, 2$, namely, $m = 2$ (blue line), and $n = 1, 2, 3$, namely, $m = 3$ (green line), in (a)/(b) and (f)/(h) linear combination of the data for $m = 2$ (blue line) and $m = 3$ (green line) in (a)/(b). The results for $m = 2$ are weighted to optimally cancel the crosstalk. The results for $m = 3$ are weighted to cancel not only the crosstalk but also the lower-frequency background.

Next, the case of $m = 3$ is considered using Eq. (A14) of Appendix A, Eq. (B1) of Appendix B 1, and Eq. (B11) of Appendix B 2 to cancel the very low frequency component in addition to the counterpart-frequency component. The equation to be solved is as follows:

$$\begin{pmatrix} 1 & 1 & 1 \\ 1 & -1 & 1 \\ G_1^{ss}(x_1) & G_2^{ss}(x_1) & G_3^{ss}(x_1) \end{pmatrix} \begin{pmatrix} a_1 \\ a_2 \\ a_3 \end{pmatrix} = \begin{pmatrix} 1 \\ 0 \\ 0 \end{pmatrix}. \qquad (2)$$

Here, 31.25/20 (20/31.25) is also chosen as x_1 for sample A (B), and $a_1 = 0.186$ (-0.153), $a_2 = 0.5$ (0.5), and $a_3 = 0.314$ (0.653) are obtained, respectively.

Figures 13(k) and 13(l) show the results of the weighted sum of the data obtained by analyzing one and two periods, with the corresponding FFTs shown in Figs. 15(k) and 15(l). From these, it can be seen that in addition to 11.25 kHz, the frequency component at 20 kHz (31.25 kHz) is also significantly reduced compared to the data before the linear combination. The corresponding passing gains

G_{total}^{cc} and G_{total}^{ss} for the Au (Ag) wire measurements for the case of $m = 3$ are shown in Figs. 16(e) and 16(f) [Figs. 16(g) and 16(h)], respectively. The values of both of G_{total}^{cc} and G_{total}^{ss} for $m = 3$ are also 1 and 0 at 20 kHz and 31.25 kHz (31.25 kHz and 20 kHz) for Au (Ag) wire measurements, respectively. In addition, the values of G_{total}^{cc} and G_{total}^{ss} for $m = 3$ at lower frequencies become far closer to zero than those for $m = 2$. In Figs. 13(k) and 13(l), the oscillation at lower magnetic fields is well suppressed, in addition to the suppression of the oscillation at higher fields.

According to the OFDM concept, when removing a component of 31.25 kHz (20 kHz) from a signal with a modulation frequency of 20 kHz (31.25 kHz), the data over a time of 800 μs [i.e., 16 (25) periods] are required. However, employing the concept shown in Figs. 1(c) and 1(d), these frequencies can be removed by integrating data over two periods (100 μs and 64 μs, respectively), which is considerably shorter than required for the OFDM concept (see Fig. 17). Thus, this proposed method is a promising and powerful tool for signal demodulation.

4. Using identical samples of the silver wire, we prepared the wiring shown in the circuit diagrams of Fig. 18(a) and Fig. 18(e). We randomly moved the external coaxial cables and then measured three times in zero magnetic field at 78 K for both setups. The results are shown in Figs. 18(b)–18(d) and 18(f)–18(h) for single-ended and differential signaling, respectively. Although the real parts of the signals are reproducible, the imaginary part is not when using the single-ended method. This is the definitive proof that the differential method is overwhelmingly superior to the single-ended method.

5. Figures 19(a) and 19(b) show the phase shift of the voltage across the shunt resistor if the reference oscillators of the oscilloscope and the function generator are synchronized, or not. We used a modulation frequency of 25 kHz and a silver wire as a sample. In the case of synchronization, small steps appear, which may be a phenomenon specific to this oscilloscope. On the other hand, in the asynchronous case, the phase
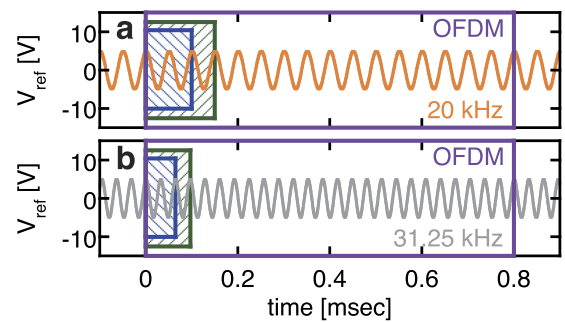

FIG. 17. Experimental value of the voltage over a shunt resistor in ⟨3⟩ of *Measurement I*. It takes 0.8 ms for both frequencies of (a) 20 kHz (gold wire) and (b) 31.25 kHz (silver wire) waves to return to the same phase. Whereas the conventional OFDM method requires 0.8 ms to separate the two signals (purple rectangle), the method for $m = 2$ in Figs. 16(e)–16(h) requires only 0.1 ms and 0.064 ms (blue rectangles), respectively. Even if low-frequency components are removed in the case of $m = 3$ [Figs. 16(e)–16(h)], only 0.15 ms and 0.096 ms (green rectangles) are required, respectively.
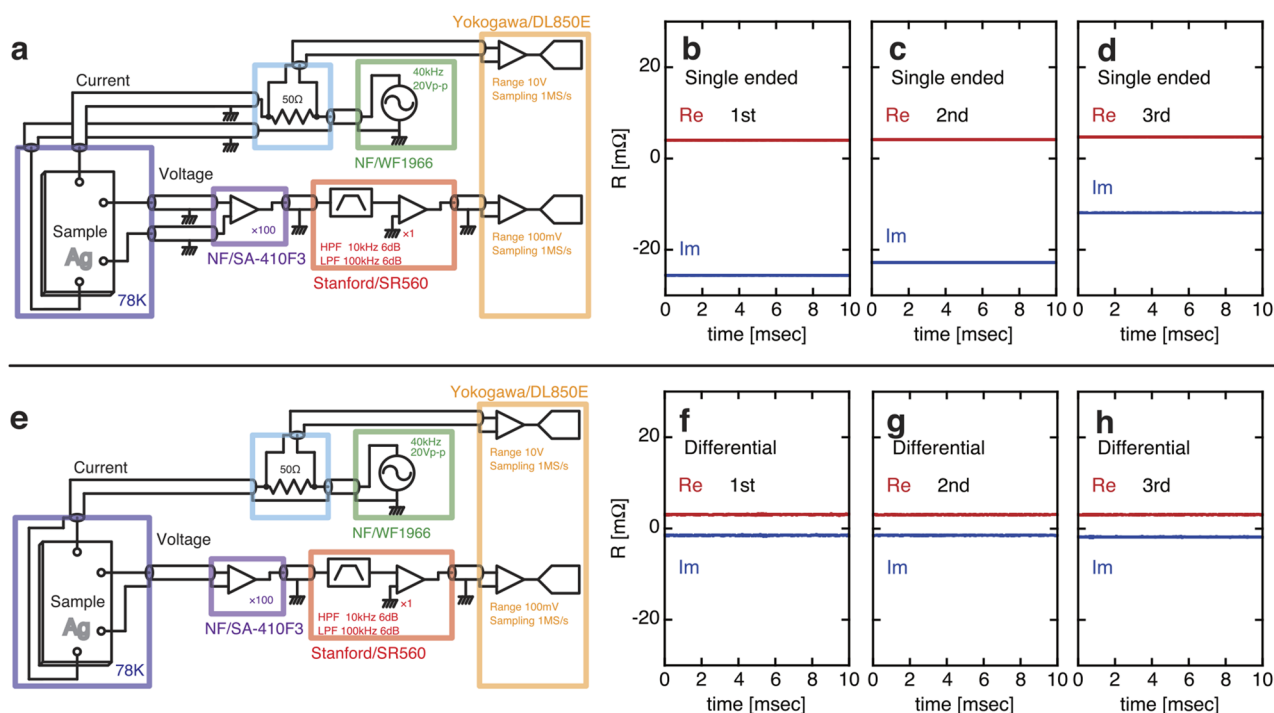
FIG. 18. (a) The circuit diagram for single-ended signaling and (b)–(d) the results of three times repeating the successive operations of randomly moving the coaxial cables and measuring the Ag sample's resistance. (e) The circuit diagram for differential signaling and (f)–(h) the results of three times repeating the successive operations of randomly moving the coaxial cables and measuring the Ag sample's resistance.

shift changes almost linearly with time. When considering the phase-shift correction method for these results, it seems that the asynchronous case will be easier to process.

6. We investigated the influence of mechanical noise under three conditions. The results are shown in Figs. 20(b)–20(d), respectively. The noise is largest when the SUS304 pipe is attached to the tip of the probe, especially for increasing fields. The data shown in Fig. 20(b) are slightly noisier than those shown in Fig. 20(d). This may be related to the fact that stainless-steel Dewars are used in Yokohama and Dresden, while glass Dewars are used in Kashiwa. In any way, it is clear that eddy currents in metal tubes are the cause of mechanical vibrations.
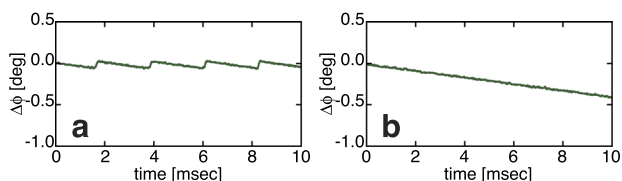

FIG. 19. Experimental results of the phase shift of a 25 kHz signal generated by the function generator with respect to the oscilloscope in the case of (a) synchronous and (b) asynchronous detection, respectively.

b. Measurement II.

7. The measured voltage over a platinum wire in a magnetic field up to 11 T without a magnetic-flux compensation coil or bandpass filter is shown in Fig. 21(b). The amplitude of the component oscillating at the modulation frequency is considerably smaller than the component corresponding to dB/dt in Fig. 20(a). This means that the measurement is performed in a much larger range than required for the signal originating from the sample, which is discarding the information of the lower bits of the oscilloscope's AD converter. Applying numerical phase detection using one modulation period, the result shown in Fig. 21(c) is obtained. It can be easily seen that fluctuations are superimposed on the signal derived from the sample. In this case, the dB/dt component in the output voltage has a very low frequency of about 45 Hz and a very large amplitude; hence, the mixing frequency with the 25 kHz modulation is not effectively removed by the numerical phase detection. For these two reasons, it is essential to remove this large dB/dt component superimposed on the signal before digitizing it by the AD converter in the oscilloscope. The possible methods for suppressing the dB/dt component from the sample's signal are as follows: subtracting the voltage obtained by a magnetic-flux compensation coil [Figs. 21(g) and 21(h)], using a high-pass filter [Figs. 21(d) and 21(e)], or a combination of both methods [Figs. 21(i) and 21(j)], respectively. Although these methods display differences in the noise level, they all
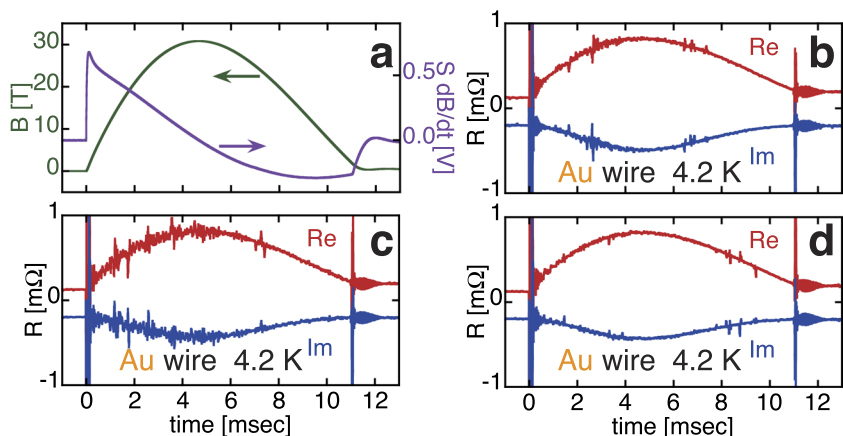
FIG. 20. Difference in mechanical noise depending on how the probe is fixed inside a glass Dewar and in the center of the magnet. (a) The magnetic pulse profile and its time derivative, measured using the voltage of the field pickup coil. (b) Real and imaginary parts of the detected signal of a gold wire with the Teflon tape wrapped around the tip of the probe so that it just fits inside the Dewar. (c) The signal when a SUS304 pipe with an outer diameter of 8 mm, a wall thickness of 0.5 mm, and a length of 61 mm is attached to the tip of the probe. (d) The signal without anything attached to the tip of the probe.

are a very effective means to lower the oscilloscope's dynamic range (and increase its resolution) and suppress the ringing out due to dB/dt. The results in quasi-static magnetic fields up to 12 T by using a PPMS are also shown in Fig. 21(e) as a green line. The results in pulsed-magnetic fields are consistent with those in quasi-static-magnetic fields.

c. Measurement III.

8. The magnetoresistance of a sample with loosely fixed wirings is shown in Fig. 22(a) for measurements using the DC and AC method. Their results differ largely, although there is no noise detected. Next, the wiring around the sample was further fixed and the sample was measured again. Now, both
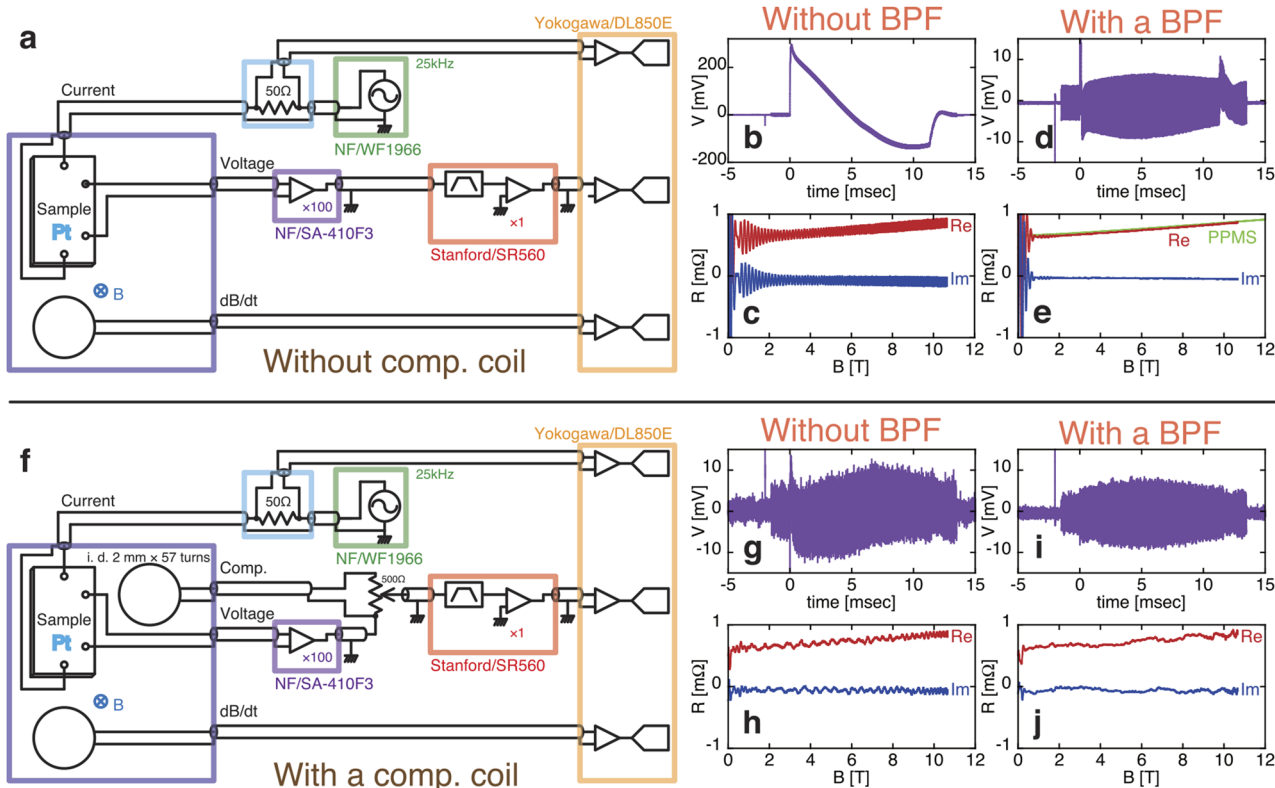
FIG. 21. Circuit diagram (a) without and (f) with a compensation coil, and the corresponding data of V vs time in (b)/(d) and (g)/(i), respectively, and of R vs B in (c)/(e) and (h)/(j), respectively, without/with a bandpass filter (BPF) for a platinum wire. The red and blue lines show the real and imaginary parts, respectively. The green line in (e) shows the measurement results in quasi-static magnetic fields by using a PPMS.
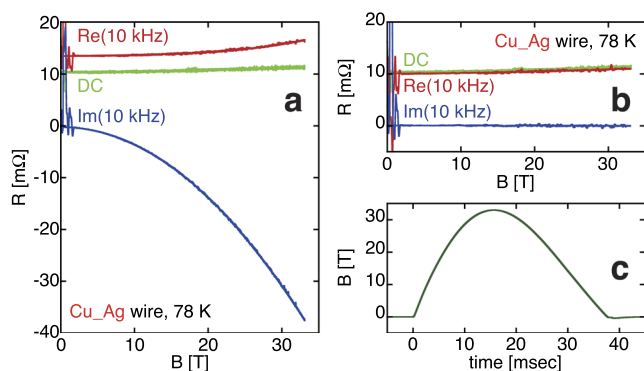
FIG. 22. (a) Resistance data when the wiring around the sample is loosely fixed. There is a discrepancy in the results between AC (10 kHz) and DC excitation. (b) Resistance data after further reinforcing the fixation of the wiring. The results of DC and AC (10 kHz) measurements match very well. (c) Waveform of the pulsed magnetic field used in this experiment.

the AC and DC results are in good agreement with each other as well as with the previous DC method, as shown in Fig. 22(b). As the Lorentz force on the AC current in the wiring causes a mechanical vibration with a frequency in the same range as the applied modulation frequency, it is nearly impossible for any signal processing technology to separate such components from the actual signal of interest.

IV. SUMMARY

In the present study, we have realized a very high resolution in electrical transport measurements performed in pulsed magnetic fields by introducing a numerical phase-detection technique. The impedance due to the mutual inductance around the sample can be suppressed to several microhms using a low modulation frequency. In addition, we were able to reduce a reproducible background signal by measuring a sample twice with opposite AC-current polarities. This was achieved by an excellent frequency stability of the TCXOs used in the frequency generator and storage oscilloscope.

In AC measurements, handling of the phase shift is challenging. We have additionally devised a correction method for this phase shift in AC measurements and demonstrated its validity for actual data. Generally, the simultaneous measurement of multiple samples leads to the interference of the used modulation frequencies. We have addressed this problem and give guidance to avoid such interference. Utilizing these techniques, we consider that the magnetoresistance and Hall resistance of various highly conductive metallic samples will be easily and extensively measured in pulsed high magnetic fields in the future.

The well-defined noise, seen in FFT analysis, is often due to mechanical eigenfrequencies of the probe (and magnet). This is considered to be induced by the electromotive force generated by the mechanical oscillation of the loop part of the wiring in a non-uniform magnetic field. In order to reduce such noise, a new technique of numerical phase detection was developed. These techniques are expected to be applied not only to transport measurements in pulsed magnetic fields but also to various other transient measurements.

On the other hand, if mechanical vibrations can be suppressed well, it can be said that long magnetic-field pulses are not necessarily required for accurate measurements. Indeed, our method has sufficient temporal resolution for existing pulsed magnets. A short pulse duration rather allows us to apply a large current during the pulse increasing the signal-to-noise ratio.

APPENDIX A: GENERAL FORMULA

The fundamental concept of phase detection is to extract the desired quantity by multiplying the oscillating signal [Fig. 23(a)] with $2 \cos \omega_0 t$ [Fig. 23(b)] or $2 \sin \omega_0 t$ [Fig. 23(c)], when the angular frequency of the modulated signal is set to ω_0. Assuming that the signal $f(t)$ is

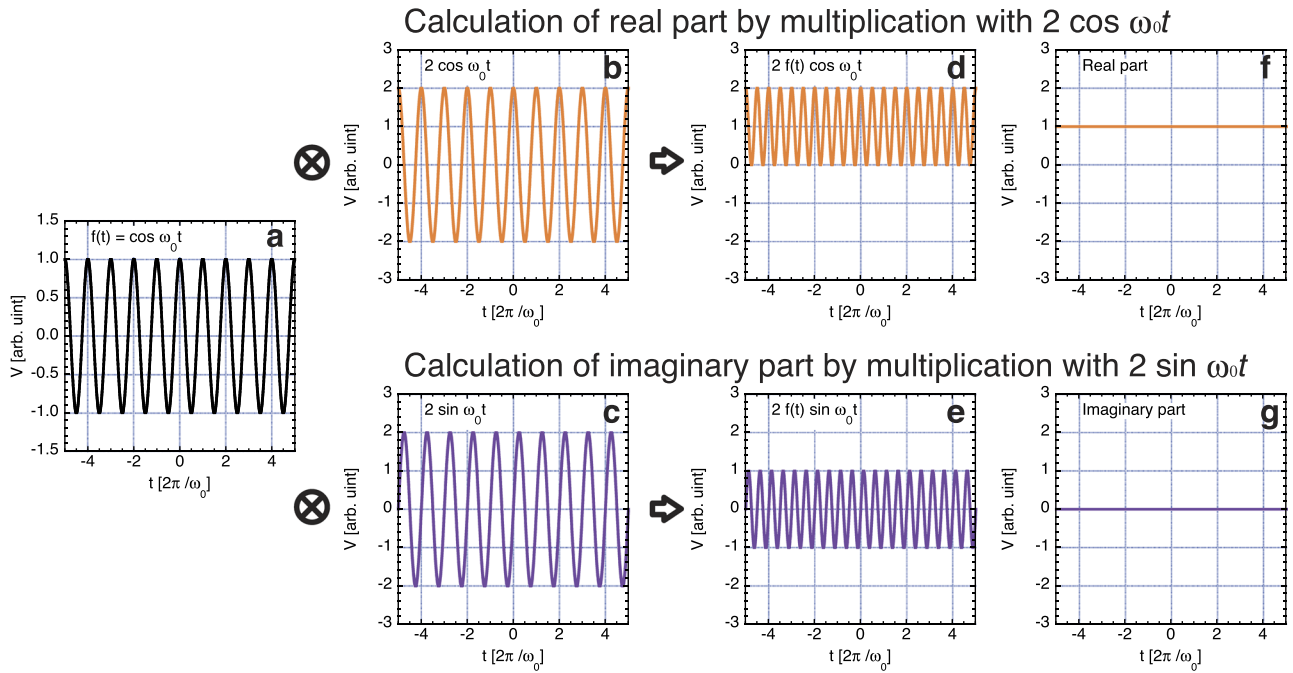$$f(t) \equiv A \cos \omega_0 t + B \sin \omega_0 t, \tag{A1}$$

then $f(t) \times 2 \cos \omega_0 t$ and $f(t) \times 2 \sin \omega_0 t$ become

$$f(t) \times 2 \cos \omega_0 t = A(1 + \cos 2\omega_0 t) + B \sin 2\omega_0 t, \tag{A2}$$

$$f(t) \times 2 \sin \omega_0 t = A \sin 2\omega_0 t + B(1 - \cos 2\omega_0 t), \tag{A3}$$

respectively [Figs. 23(d) and 23(e)].

If the terms of $\cos 2\omega_0 t$ and $\sin 2\omega_0 t$, which are second-harmonic oscillations, are successfully removed, the values of A and B are obtained as components independent of time. In the analog method, since these terms are removed by a low-pass filter, one needs a far longer integration time than just one period of the modulation frequency [Figs. 23(f) and 23(g)]. In the numerical phase-detection method (the so-called digital method), however, second-harmonic oscillations can be eliminated with a very short integration

Calculation of real part by multiplication with $2\cos\omega_0 t$

Calculation of imaginary part by multiplication with $2\sin\omega_0 t$

FIG. 23. The fundamental principle of the numerical phase detection. When the detected signal (a) is multiplied by a cosine wave (b) and a sine wave (c) with the same frequency, a mixed signal with twice the original frequency appears in the real (d) and imaginary (e) parts, respectively. When using moving averages with an interval of integral multiples of the oscillation period, only the real (f) and imaginary (g) parts of the signal remain.

time by using the relations

$$\frac{\omega_0}{2n\pi} \int_{-\frac{n\pi}{\omega_0}}^{+\frac{n\pi}{\omega_0}} \cos 2\omega_0 t\, dt = 0 \ (n = 1, 2, 3, \ldots), \tag{A4}$$

$$\frac{\omega_0}{2n\pi} \int_{-\frac{n\pi}{\omega_0}}^{+\frac{n\pi}{\omega_0}} \sin 2\omega_0 t\, dt = 0 \ (n = 1, 2, 3, \ldots), \tag{A5}$$

$$\frac{\omega_0}{2n\pi} \int_{-\frac{n\pi}{\omega_0}}^{+\frac{n\pi}{\omega_0}} 1\, dt = 1 \ (n = 1, 2, 3, \ldots), \tag{A6}$$

i.e., by selecting the integration interval as an integral multiple of one period. Here, the pass gains (G_n^{cc}: real part, G_n^{ss}: imaginary part, G_n^{sc} and G_n^{cs}: off-diagonal components) for the general angular frequency ω are given by

$$G_n^{cc}\left(\frac{\omega}{\omega_0}\right) \equiv \frac{\omega_0}{2n\pi} \int_{-\frac{n\pi}{\omega_0}}^{+\frac{n\pi}{\omega_0}} \cos\omega t \times 2\cos\omega_0 t\, dt$$

$$= \begin{cases} \frac{(-1)^{n-1}}{n\pi} \frac{2\left(\frac{\omega}{\omega_0}\right)}{1-\left(\frac{\omega}{\omega_0}\right)^2} \sin n\pi\left(\frac{\omega}{\omega_0}\right) & \left(\frac{\omega}{\omega_0} \neq 1\right) \\ 1 & \left(\frac{\omega}{\omega_0} = 1\right), \end{cases} \tag{A7}$$

$$G_n^{sc}\left(\frac{\omega}{\omega_0}\right) \equiv \frac{\omega_0}{2n\pi} \int_{-\frac{n\pi}{\omega_0}}^{+\frac{n\pi}{\omega_0}} \sin\omega t \times 2\cos\omega_0 t\, dt$$

$$= 0, \tag{A8}$$

$$G_n^{ss}\left(\frac{\omega}{\omega_0}\right) \equiv \frac{\omega_0}{2n\pi} \int_{-\frac{n\pi}{\omega_0}}^{+\frac{n\pi}{\omega_0}} \sin\omega t \times 2\sin\omega_0 t\, dt$$

$$= \begin{cases} \frac{(-1)^{n-1}}{n\pi} \frac{2}{1-\left(\frac{\omega}{\omega_0}\right)^2} \sin n\pi\left(\frac{\omega}{\omega_0}\right) & \left(\frac{\omega}{\omega_0} \neq 1\right) \\ 1 & \left(\frac{\omega}{\omega_0} = 1\right), \end{cases} \tag{A9}$$
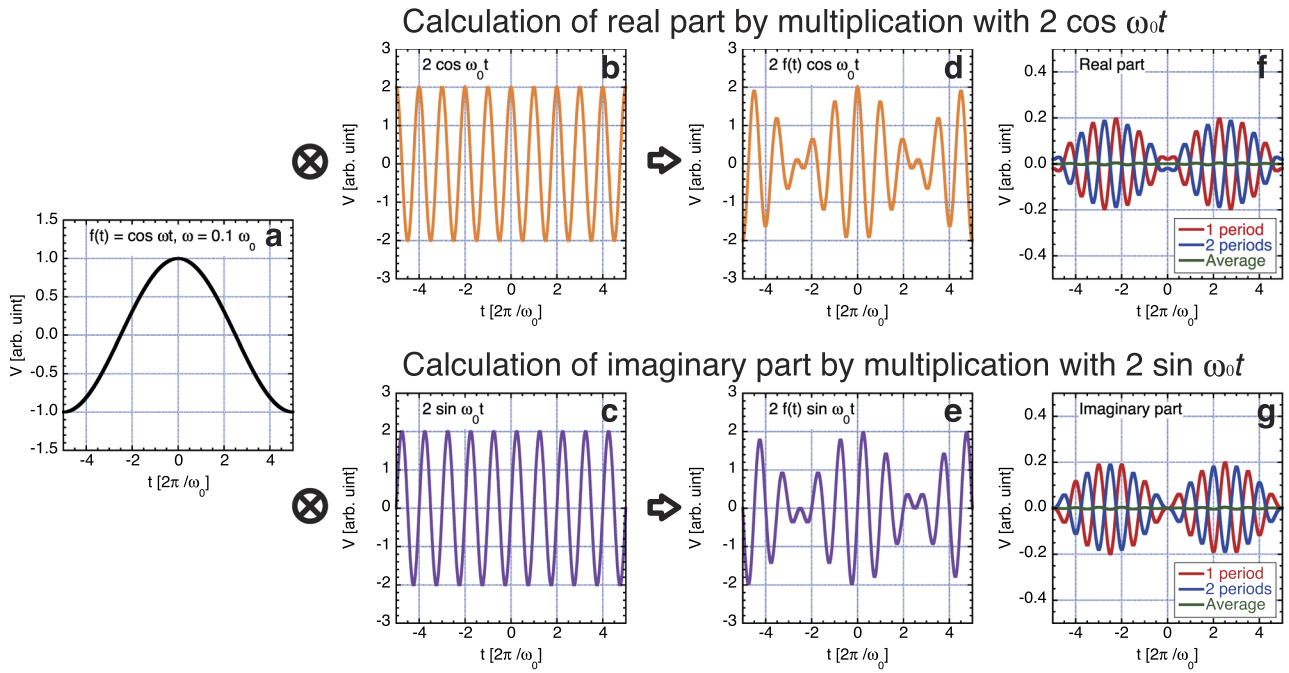
$$G_n^{cs}\left(\frac{\omega}{\omega_0}\right) \equiv \frac{\omega_0}{2n\pi} \int_{-\frac{n\pi}{\omega_0}}^{+\frac{n\pi}{\omega_0}} \cos\omega t \times 2\sin\omega_0 t\, dt$$

$$= 0, \tag{A10}$$

with the integration time of n periods of the angular modulation frequency ω_0. Here, we set $x \equiv \omega/\omega_0$ to obtain a dimensionless angular frequency. $G_n^{sc}(x)$ and $G_n^{cs}(x)$ are identical to zero and $G_n^{cc}(x)$ and $G_n^{ss}(x)$, for $n = 1, 2, 3, 4,$ and 5, are shown in Figs. 1(a) and 1(b), respectively. The envelope (amplitude) of the actual passing waveform for a specific angular frequency oscillates between the values of $G_n^{cc}(x)$ and $G_n^{ss}(x)$ (see Fig. 24).

As can be seen from Figs. 1(a) and 1(b), the performance of eliminating noise, considered as an advantage of phase detection, rapidly becomes worse as the integration time becomes shorter. Therefore, when using the numerical method, if n is very small, we must consider a noise elimination method separately.

Generally, there are various sources of noise, but often the noise appears at a specific frequency, as discussed in the main text. Therefore, we newly devised a method for efficiently removing specific frequency components by numerical phase detection using data

Calculation of real part by multiplication with $2\cos\omega_0 t$

Calculation of imaginary part by multiplication with $2\sin\omega_0 t$

FIG. 24. The case of forced demodulation of a target signal of a frequency different from that of the reference signal. (a) Target signal with a frequency of one tenth of the reference signal. The target signal multiplied by a cosine wave (b) and a sine wave (c) results in the signals (d) and (e), respectively. The results (f) and (g) of the averaging operation strongly depend on the integer value (1—red lines, 2—blue lines, . . .) that determines the possible intervals. In this case, taking the average (green lines) of the red and blue lines suppresses the oscillations considerably. This mechanism corresponds to the case of $m = 2$ in Appendix B 2.

over a limited time range. We have noticed that the characteristic frequency dependence of the pass gain depends on n. Furthermore, we have found that an excellent filtering function can be realized by taking a linear combination of pass gains with different n. By that, unwanted phase shift does not occur in the obtained signal. Here, the total pass gain [$G_{total}^{cc}(x)$ and $G_{total}^{ss}(x)$], by taking a linear combination of the results of phase detection using data from one to m periods, is shown in the following:

$$G_{total}^{cc}(x) \equiv a_1 G_1^{cc}(x) + a_2 G_2^{cc}(x) + \cdots + a_m G_m^{cc}(x), \tag{A11}$$

$$G_{total}^{ss}(x) \equiv a_1 G_1^{ss}(x) + a_2 G_2^{ss}(x) + \cdots + a_m G_m^{ss}(x). \tag{A12}$$

Generally, there is the relation

$$G_n^{cc}(1) = G_n^{ss}(1) = 1, \ (n = 1, 2, 3, \ldots, m). \tag{A13}$$

If the condition

$$a_1 + a_2 + \cdots + a_m = 1 \tag{A14}$$

is imposed, the relation

$$G_{total}^{cc}(1) = G_{total}^{ss}(1) = 1 \tag{A15}$$

is automatically established. In order to determine the values of a_1, a_2, . . ., a_m, here, $m - 1$ equations are required. The choice of the filter function depends on the conditions imposed on a_1, a_2, . . ., a_m.

APPENDIX B: EXAMPLES

The presented method is an extremely powerful tool for reducing the noise at a specific frequency within a very short time by using numerical phase detection. As an example, a method for constructing a multi-frequency notch filter, a high-pass filter, and a higher-order notch filter is provided below.

1. Multi-frequency notch filter

When the angular frequencies $\omega_i \equiv x_i \omega_0$, $(x_i \neq 1)$ of the noise to be removed are discrete and have a finite number ($\mu - 1$),

$$G_{total}^{ss}(x_i) = 0 \ (i = 1, 2, 3, \ldots, \mu - 1) \tag{B1}$$

should be imposed. From Eqs. (A7) and (A9), generally, the relation

$$G_n^{cc}(x) = x G_n^{ss}(x) \ (n = 1, 2, 3, \ldots, m) \tag{B2}$$

holds. Therefore,

$$G_{total}^{cc}(x) = x G_{total}^{ss}(x) \tag{B3}$$

is established. If x_i is the relative, dimensionless noise frequency to be eliminated, then

$$G_{total}^{ss}(x_i) = 0 \Rightarrow G_{total}^{cc}(x_i) = 0 \ (i = 1, 2, 3, \ldots, \mu - 1) \tag{B4}$$

holds. Thus, we only need to consider the zero points of $G_{total}^{ss}(x)$. We can write these equations together in the form of matrices as

$$\begin{pmatrix} 1 & 1 & \cdots & 1 \\ G_1^{ss}(x_1) & G_2^{ss}(x_1) & \cdots & G_m^{ss}(x_1) \\ G_1^{ss}(x_2) & G_2^{ss}(x_2) & \cdots & G_m^{ss}(x_2) \\ \vdots & \vdots & \ddots & \vdots \\ G_1^{ss}(x_{\mu-1}) & G_2^{ss}(x_{\mu-1}) & \cdots & G_m^{ss}(x_{\mu-1}) \end{pmatrix} \begin{pmatrix} a_1 \\ a_2 \\ \vdots \\ a_m \end{pmatrix} = \begin{pmatrix} 1 \\ 0 \\ 0 \\ \vdots \\ 0 \end{pmatrix}. \quad \text{(B5)}$$

This simultaneous linear equation for $a_1, a_2, \ldots a_m$ can be easily solved numerically. As a result, numerical phase detection with a notch-filter function for arbitrary and known angular frequency ω_i ($\neq \omega_0$) ($i = 1, \ldots, \mu - 1$) is realized by using only the short-time data of at most $2 m\pi/\omega_0 t$ without resulting in any additional phase shift of the signal (see Fig. 25).

2. High-pass filter

When $G_n^{cc}(x)$ of Eq. (A7) and $G_n^{ss}(x)$ of Eq. (A9) are expanded into a power series with respect to x around $x = 0$,

$$\begin{aligned} G_n^{cc}(x) &= 2(-1)^{n-1} \cdot \frac{x}{1-x^2} \cdot \frac{1}{n\pi} \sin n\pi x \\ &= 2(-1)^{n-1} \cdot (x + x^3 + x^5 + \cdots)\left(x - \frac{n^2\pi^2}{3!}x^3 + \frac{n^4\pi^4}{5!}x^5 + \cdots\right) \\ &= 2(-1)^{n-1} \cdot \left\{x^2 + \left(1 - \frac{n^2\pi^2}{3!}\right)x^4 \right. \\ &\quad \left. + \left(1 - \frac{n^2\pi^2}{3!} + \frac{n^4\pi^4}{5!}\right)x^6 + \cdots\right\}, \end{aligned} \quad \text{(B6)}$$

$$\begin{aligned} G_n^{ss}(x) &= 2(-1)^{n-1} \cdot \frac{1}{1-x^2} \cdot \frac{1}{n\pi} \sin n\pi x \\ &= 2(-1)^{n-1} \cdot (1 + x^2 + x^4 + \cdots)\left(x - \frac{n^2\pi^2}{3!}x^3 + \frac{n^4\pi^4}{5!}x^5 + \cdots\right) \\ &= 2(-1)^{n-1} \cdot \left\{x + \left(1 - \frac{n^2\pi^2}{3!}\right)x^3 \right. \\ &\quad \left. + \left(1 - \frac{n^2\pi^2}{3!} + \frac{n^4\pi^4}{5!}\right)x^5 + \cdots\right\} \end{aligned} \quad \text{(B7)}$$

are obtained. Here, we should emphasize that the coefficient of each lowest-order term is $2(-1)^{n+1}$, so it does not converge to zero even at the limit of $n \to \infty$. This means that even if the time domain of the integral is simply increased, it is difficult to suppress noise of the lower limit frequency. However, if we assume $a_1 = 1/2$ and $a_2 = 1/2$ when $m = 2$, Eqs. (A11), (A12), (B6), and (B7) give

$$\begin{aligned} G_{total}^{cc}(x) &= a_1 G_1^{cc}(x) + a_2 G_2^{cc}(x) \\ &= \frac{1}{2} \cdot 2\left\{x^2 + \left(1 - \frac{\pi^2}{3!}\right)x^4 + \cdots\right\} \\ &\quad - \frac{1}{2} \cdot 2\left\{x^2 + \left(1 - \frac{4\pi^2}{3!}\right)x^4 + \cdots\right\} \\ &= \frac{\pi^2}{2}x^4 + \cdots, \end{aligned} \quad \text{(B8)}$$
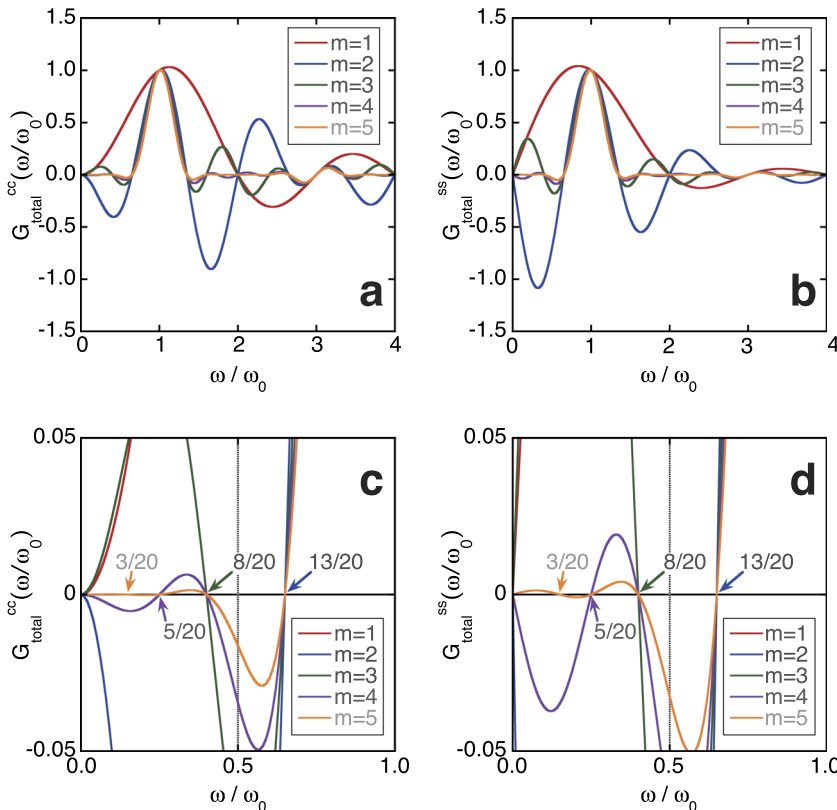
FIG. 25. The implementation example of a multi-frequency notch filter that removes the frequency components at $m - 1$ points ($m = 2, 3, 4,$ and 5). As an example, the frequency components to be removed are chosen as the order of $x = 13/20, 8/20, 5/20,$ and $3/20$. The coefficients can be easily determined by substituting numerical values into Eq. (B5). (a) and (b) show the real (G_{total}^{cc}) and imaginary (G_{total}^{ss}) parts of the frequency dependence of the pass gain, respectively. (c) and (d) are the enlarged views of (a) and (b), respectively.

$$G_{total}^{ss}(x) = a_1 G_1^{ss}(x) + a_2 G_2^{ss}(x)$$
$$= \frac{1}{2} \cdot 2 \left\{ x + \left(1 - \frac{\pi^2}{3!}\right) x^3 + \cdots \right\}$$
$$- \frac{1}{2} \cdot 2 \left\{ x + \left(1 - \frac{4\pi^2}{3!}\right) x^3 + \cdots \right\}$$
$$= \frac{\pi^2}{2} x^3 + \cdots. \tag{B9}$$

In this way, we can eliminate the lowest-order terms while keeping the constraint of Eq. (A15). Therefore, although the time domain required for the integration is the same, this method can much more efficiently reduce low-frequency noise than simple data integration for $n = 2$. If this idea is further expanded, coefficients of arbitrary degree can be erased. When considering $G_n^{ss}(x)$, $G_n^{cc}(x)$ is also automatically optimized because of Eq. (B3). If $m \geq 2$,

$$G_{total}^{ss}(x) = a_1 G_1^{ss}(x) + a_2 G_2^{ss}(x) + \cdots + a_m G_m^{ss}(x)$$
$$= \frac{2}{1 - x^2} \left[\left\{ a_1 - a_2 + \cdots + (-1)^{m+1} a_m \right\} x \right.$$
$$- \frac{\pi^2}{3!} \left\{ 1^2 a_1 - 2^2 a_2 + \cdots + (-1)^{m+1} m^2 a_m \right\} x^3$$
$$\left. + \frac{\pi^4}{5!} \left\{ 1^4 a_1 - 2^4 a_2 + \cdots + (-1)^{m+1} m^4 a_m \right\} x^5 \cdots \right] \tag{B10}$$

is obtained from Eqs. (A9) and (A12). If we assume

$$a_1 - a_2 + a_3 + \cdots + (-1)^{m+1} a_m = 0,$$
$$1^2 a_1 - 2^2 a_2 + 3^2 a_3 + \cdots + (-1)^{m+1} m^2 a_m = 0, \tag{B11}$$
$$1^4 a_1 - 2^4 a_2 + 3^4 a_3 + \cdots + (-1)^{m+1} m^4 a_m = 0 \cdots,$$

the coefficients of all terms from x to x^{2m-1} are 0 in Eq. (B10). We obtain the following simultaneous linear equations:

$$\begin{pmatrix} 1 & 1 & \cdots & 1 \\ 1 & -1 & \cdots & (-1)^{m+1} \\ 1^2 & -2^2 & \cdots & (-1)^{m+1} m^2 \\ \vdots & \vdots & \ddots & \vdots \\ 1^{2m-4} & -2^{2m-4} & \cdots & (-1)^{m+1} m^{2m-4} \end{pmatrix} \begin{pmatrix} a_1 \\ a_2 \\ a_3 \\ \vdots \\ a_m \end{pmatrix} = \begin{pmatrix} 1 \\ 0 \\ 0 \\ \vdots \\ 0 \end{pmatrix} \tag{B12}$$

by combining Eq. (A14). The solutions are

$$m = 2 \Rightarrow a_1 = \frac{1}{2}, a_2 = \frac{1}{2},$$
$$m = 3 \Rightarrow a_1 = \frac{5}{16}, a_2 = \frac{1}{2}, a_3 = \frac{3}{16},$$
$$m = 4 \Rightarrow a_1 = \frac{7}{32}, a_2 = \frac{7}{16}, a_3 = \frac{9}{32}, a_4 = \frac{1}{16}, \tag{B13}$$
$$m = 5 \Rightarrow a_1 = \frac{21}{128}, a_2 = \frac{3}{8}, a_3 = \frac{81}{256}, a_4 = \frac{1}{8}, a_5 = \frac{5}{256} \cdots.$$

When G_{total}^{cc} and G_{total}^{ss} are expanded in a series of power x, the lowest order of G_{total}^{ss} is lower than that of G_{total}^{cc}. Thus, the property of G_{total}^{ss} dominates the performance of this filter. As a result, numerical phase detection with a function of the $(2m - 1)$th order high-pass filter can be realized using only the data of the time width of at most $2m\pi/\omega_0 t$ without any phase shift of the signal. Figure 26 shows the

pass gains of the concrete real and imaginary parts. In other words, we can give the G_{total}^{cc} and G_{total}^{ss} superior character not found in the original G_n^{cc} and G_n^{ss}.

3. Higher-order notch filter

Here, we consider a higher-order notch filter to remove noise distributed with a certain width around $x = x_1$. When the conditions

$$G_{total}^{ss}(x_1) = G_{total}^{cc}(x_1)$$
$$= G_{total}^{ss}{}'(x_1) = G_{total}^{cc}{}'(x_1)$$
$$= G_{total}^{ss}{}''(x_1) = G_{total}^{cc}{}''(x_1) \tag{B14}$$
$$\cdots$$
$$= G_{total}^{ss}{}^{(l)}(x_1) = G_{total}^{cc}{}^{(l)}(x_1) = 0$$

are imposed, an lth order notch filter is realized. Since the relations

$$G_{total}^{cc}{}'(x) = G_{total}^{ss}(x) + x G_{total}^{ss}{}'(x)$$
$$G_{total}^{cc}{}''(x) = 2 G_{total}^{ss}{}'(x) + x G_{total}^{ss}{}''(x)$$
$$G_{total}^{cc}{}'''(x) = 3 G_{total}^{ss}{}''(x) + x G_{total}^{ss}{}'''(x) \tag{B15}$$
$$\cdots$$
$$G_{total}^{cc}{}^{(l)}(x) = l G_{total}^{ss}{}^{(l-1)}(x) + x G_{total}^{ss}{}^{(l)}(x)$$

are established from Eq. (B3), the relations

$$G_{total}^{ss}(x_1) = G_{total}^{ss}{}'(x_1)$$
$$= G_{total}^{ss}{}''(x_1) = \cdots = G_{total}^{ss}{}^{(l)}(x_1) = 0$$
$$\Rightarrow G_{total}^{cc}(x_1) = G_{total}^{cc}{}'(x_1) \tag{B16}$$
$$= G_{total}^{cc}{}''(x_1) = \cdots = G_{total}^{cc}{}^{(l)}(x_1) = 0$$

hold identically. Since the equation

$$G_{total}^{ss}{}^{(j)}(x) = a_1 G_1^{ss(j)}(x) + a_2 G_2^{ss(j)}(x)$$
$$+ a_3 G_3^{ss(j)}(x) + \cdots + a_m G_m^{ss(j)}(x) \tag{B17}$$

holds for an arbitrary integer j from Eq. (A12), the required simultaneous linear equation to determine $a_1, a_2, \ldots, a_m$ is

$$\begin{pmatrix} 1 & 1 & \cdots & 1 \\ G_1^{ss}(x_1) & G_2^{ss}(x_1) & \cdots & G_m^{ss}(x_1) \\ G_1^{ss}{}'(x_1) & G_2^{ss}{}'(x_1) & \cdots & G_m^{ss}{}'(x_1) \\ \vdots & \vdots & \ddots & \vdots \\ G_1^{ss}{}^{(l)}(x_1) & G_2^{ss}{}^{(l)}(x_1) & \cdots & G_m^{ss}{}^{(l)}(x_1) \end{pmatrix} \begin{pmatrix} a_1 \\ a_2 \\ \vdots \\ a_m \end{pmatrix} = \begin{pmatrix} 1 \\ 0 \\ 0 \\ \vdots \\ 0 \end{pmatrix}, \tag{B18}$$

where $l = m - 1$. This linear equation for $a_1, a_2, \ldots, a_m$ can be easily solved numerically, resulting in an lth-order notch-filter function that can remove the noise component of a known frequency by using the information of only the time width of at most $2m\pi/\omega_0$ without any phase rotation of the signal (see Fig. 27).

The characteristics of the newly created filters, which take a linear combination of outputs of the numerical phase detection using each integration period, are not limited to the above examples, but any combination of them is possible. Thus, this technique can remove noise at specific frequencies taking full advantage of the ability to reduce the time width required for integration with numerical phase detection.
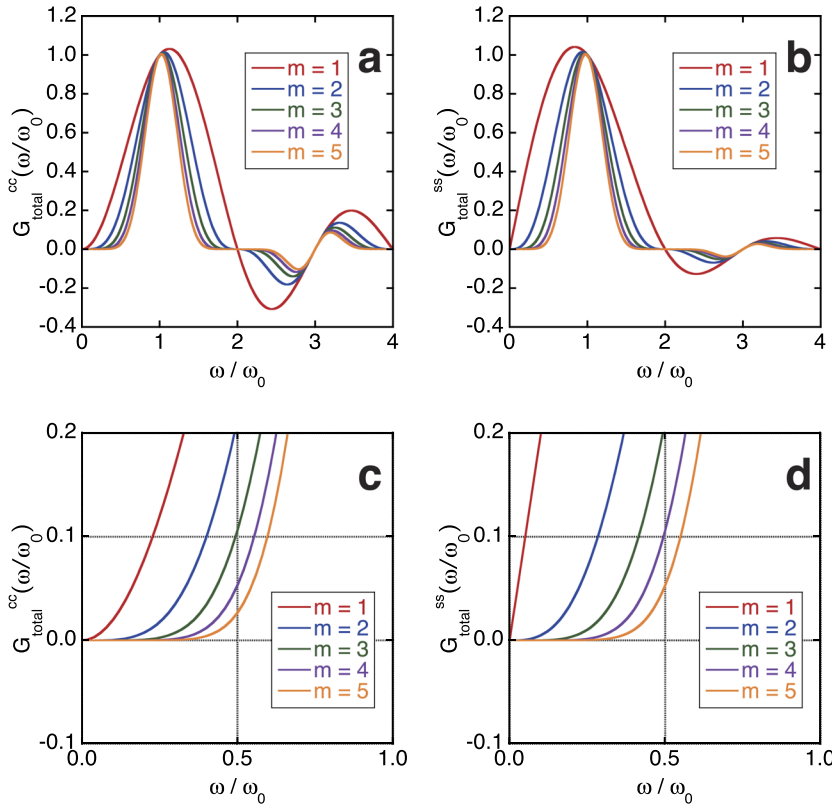
FIG. 26. Implementation example of high-pass filters. The total pass gain of $(2m - 1)$th ($m = 1, 2, 3, 4$, and 5) order high-pass filters is shown. The coefficients used are from the exact solutions (B13) obtained by solving Eq. (B12). (a) and (b) show the real (G^{cc}_{total}) and imaginary (G^{ss}_{total}) parts of the frequency dependence of the pass gain, respectively. (c) and (d) are the enlarged views of (a) and (b), respectively.

APPENDIX C: A THEOREM WITH RESPECT TO LINEAR DEPENDENCE

Since $G^{ss}_n(x)$ contains a sine function, its zero points appear periodically and infinitely. Therefore, the equations giving the zero points of $G^{ss}_{total}(x)$ may not be independent from each other. It is possible to shorten the integration time by selecting the frequency to be removed. This is quite effective when a set of frequencies to be used can be selected in advance, such as for broadband communication. The method is shown below. According to Eqs. (A9) and (A12),

$$G^{ss}_{total}(\kappa + \Delta x) = \frac{2}{1 - (\kappa + \Delta x)^2} \sum_{n=1}^{m} a_n \frac{(-1)^{n-1}}{n\pi} \sin n\pi(\kappa + \Delta x)$$
$$= \frac{2}{1 - (\kappa + \Delta x)^2} \sum_{n=1}^{m} a_n \frac{(-1)^{n-1}}{n\pi} (-1)^{n\kappa} \sin n\pi \Delta x$$

$$\text{(C1)}$$

and

$$G^{ss}_{total}(\kappa - \Delta x) = \frac{2}{1 - (\kappa - \Delta x)^2} \sum_{n=1}^{m} a_n \frac{(-1)^{n-1}}{n\pi} \sin n\pi(\kappa - \Delta x)$$
$$= -\frac{2}{1 - (\kappa - \Delta x)^2} \sum_{n=1}^{m} a_n \frac{(-1)^{n-1}}{n\pi} (-1)^{n\kappa} \sin n\pi \Delta x$$

$$\text{(C2)}$$

are obtained with regard to $x = \kappa \pm \Delta x$, $\kappa = 1, 2, 3, \ldots$ and $x \neq 1$. Therefore, the equation

$$G^{ss}_{total}(\kappa + \Delta x) = -\frac{1 - (\kappa - \Delta x)^2}{1 - (\kappa + \Delta x)^2} G^{ss}_{total}(\kappa - \Delta x) \qquad \text{(C3)}$$

holds identically. According to the above relation, the relation

$$G^{ss}_{total}(\kappa - \Delta x_i) = 0 \Rightarrow G^{ss}_{total}(\kappa + \Delta x_i) = 0, \text{ for } \kappa \pm \Delta x_i \neq 1 \qquad \text{(C4)}$$

is obtained. This means that upon removing the frequency component $\kappa - \Delta x$, the frequency component of $\kappa + \Delta x$ is also removed at the same time.

Next, we will show that the same relation generally holds for higher-order notch filters [$(l + 1)$th, $l = 0, 1, 2, \ldots$]. When we choose $f_1(\Delta x)$, $f_2(\Delta x)$, and $g(\Delta x)$ as

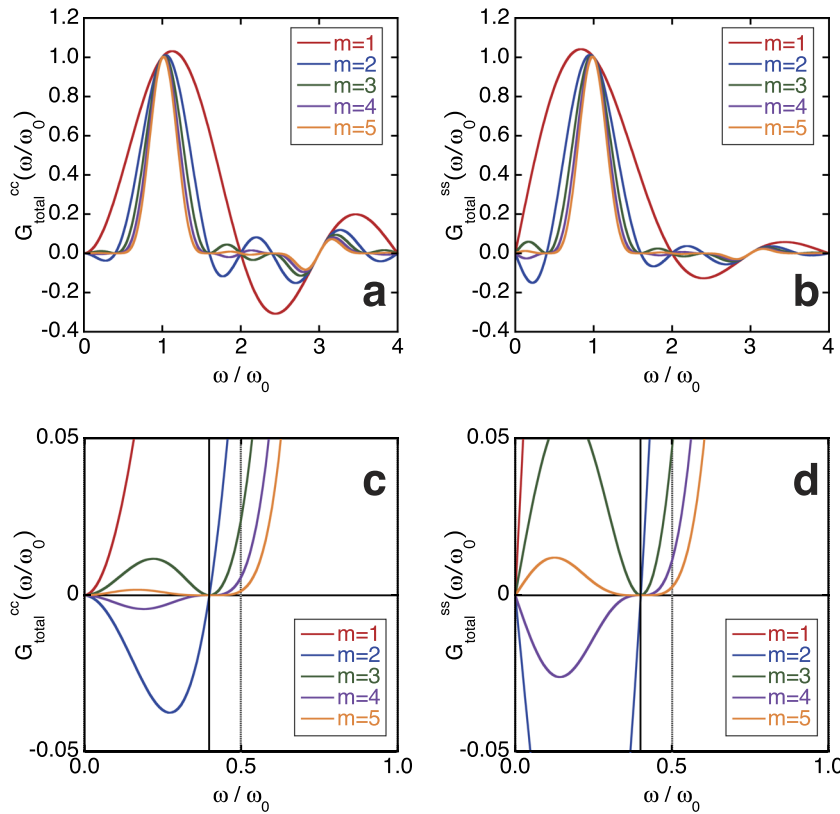$$f_1(\Delta x) \equiv G^{ss}_{total}(\kappa + \Delta x), \qquad \text{(C5)}$$

$$f_2(\Delta x) \equiv G^{ss}_{total}(\kappa - \Delta x), \qquad \text{(C6)}$$

$$g(\Delta x) \equiv -\frac{1 - (\kappa - \Delta x)^2}{1 - (\kappa + \Delta x)^2}, \qquad \text{(C7)}$$

the relation of

$$f_1(\Delta x) = g(\Delta x) f_2(\Delta x) \qquad \text{(C8)}$$

FIG. 27. Implementation example of high-order notch filters. The pass gain of the notch filter that removes the frequency component of $x = 0.4$ in the l ($= m - 1$)th order ($m = 2, 3, 4,$ and 5) is shown. The coefficients $a_1, a_2, \ldots, a_m$ can be easily determined by substituting numerical values into Eq. (B18). (a) and (b) show the real (G_{total}^{cc}) and imaginary (G_{total}^{ss}) parts of the frequency dependence of the pass gain, respectively. (c) and (d) are the enlarged views of (a) and (b), respectively.

holds without losing generality. By taking the lth derivative of Eq. (C8), we obtain

$$f_1'(\Delta x) = g'(\Delta x)f_2(\Delta x) + g(\Delta x)f_2'(\Delta x)$$

$$\cdots$$

$$f_1^{(l)}(\Delta x) = \sum_{j=0}^{l} {}_lC_j g^{(l-j)}(\Delta x)f_2^{(j)}(\Delta x). \tag{C9}$$

Thus, finally, we obtain the following relation:

$$f_2(\Delta x) = f_2'(\Delta x) = \cdots = f_2^{(j)}(\Delta x) = 0$$

$$\Rightarrow f_1(\Delta x) = f_1'(\Delta x) = \cdots = f_1^{(j)}(\Delta x) = 0 \tag{C10}$$

$$\text{for } \kappa + \Delta x_i \neq 1.$$

According to Eq. (B16), it is shown that all differential coefficients up to the lth order are zero even in the real part of the pass gain.

This means that if the function for an $(l + 1)$th order notch filter is provided for the angular frequency of $\kappa - \Delta x$, even at the frequency of $\kappa + \Delta x$, it will automatically have a function for the $(l + 1)$th order filter. In order to successfully utilize this relation, it is desirable that the respective frequencies are arranged at equal intervals and are collected on the high-frequency side within a possible frequency band. By doing so, the integration time can be further shortened.

DATA AVAILABILITY

The data that support the findings of this study are available from the corresponding author upon reasonable request.

REFERENCES

[1]S. Foner, Phys. Rev. **107**, 683 (1957).

[2]M. Date, M. Motokawa, A. Seki, S.-i. Kuroda, K.-i. Matsui, H. Nakazato, and H. Mollymoto, J. Phys. Soc. Jpn. **39**, 898 (1975).

[3]B. Meier, J. Kohlrautz, J. Haase, M. Braun, F. Wolff-Fabris, E. Kampert, T. Herrmannsdörfer, and J. Wosnitza, Rev. Sci. Instrum. **83**, 083113 (2012).

[4]H. Nojiri, M. Uchi, S. Watamura, M. Motokawa, H. Kawai, Y. Endoh, and T. Shigeoka, J. Phys. Soc. Jpn. **60**, 2380 (1991).

[5]Y. H. Matsuda, T. Inami, K. Ohwada, Y. Murata, H. Nojiri, Y. Murakami, H. Ohta, W. Zhang, and K. Yoshimura, J. Phys. Soc. Jpn. **75**, 024710 (2006).

[6]Y. H. Matsuda, T. Inami, K. Ohwada, Y. Murata, H. Nojiri, Y. Murakami, H. Ohta, W. Zhang, and K. Yoshimura, J. Phys. Soc. Jpn. **76**, 034702 (2007).

[7]E. Ohmichi and T. Osada, Rev. Sci. Instrum. **73**, 3022 (2002).

[8]J. A. Ricodeau, D. Melville, and E. W. Lee, J. Phys. E: Sci. Instrum. **5**, 472 (1972).

[9]G. Kido, Y. Tadakuma, Y. Nakagawa, Y. Nishihara, and Y. Yamaguchi, J. Magn. Magn. Mater. **54-57**, 885 (1986).

[10]R. Daou, F. Weickert, M. Nicklas, F. Steglich, A. Haase, and M. Doerr, Rev. Sci. Instrum. **81**, 033909 (2010).

[11]A. Miyake, H. Mitamura, S. Kawachi, K. Kimura, T. Kimura, T. Kihara, M. Tachibana, and M. Tokunaga, Rev. Sci. Instrum. **91**, 105103 (2020).

[12]S. Y. Dan'kov, A. M. Tishin, V. K. Pecharskya, and J. K. A. Gschneidner, Rev. Sci. Instrum. **68**, 2432 (1997).

[13]T. Kihara, Y. Kohama, Y. Hashimoto, S. Katsumoto, and M. Tokunaga, Rev. Sci. Instrum. **84**, 074901 (2013).

[14]M. Jaime, R. Movshovich, G. R. Stewart, W. P. Beyermann, M. G. Berisso, M. F. Hundley, P. C. Canfield, and J. L. Sarrao, Nature **405**, 160 (2000).

[15]Y. Kohama, C. Marcenat, T. Klein, and M. Jaime, Rev. Sci. Instrum. **81**, 104902 (2010).

[16]I. Katakura, M. Tokunaga, A. Matsuo, K. Kawaguchi, K. Kindo, M. Hitomi, D. Akahoshi, and H. Kuwahara, Rev. Sci. Instrum. **81**, 043701 (2010).

[17]B. Lax, J. G. Mavroides, H. J. Zeiger, and R. J. Keyes, Phys. Rev. **122**, 31 (1961).

[18]R. J. Keyes, S. Zwerdling, S. Foner, H. H. Kolm, and B. Lax, Phys. Rev. **104**, 1804 (1956).

[19]T. Sakai, Y. Matsumoto, and S. Mase, J. Phys. Soc. Jpn. **27**, 862 (1969).

[20]B. Wolf, B. Lüthi, S. Schmidt, H. Schwenk, M. Sieling, S. Zherlitsyn, and I. Kouroudis, Physica B **294-295**, 612 (2001).

[21]Y. F. Popov, A. M. Kadomtseva, S. S. Krotov, G. P. Vorob'ev, and M. M. Lukina, Ferroelectrics **279**, 147 (2002).

[22]H. Mitamura, S. Mitsuda, S. Kanetsuki, H. Aruga Katori, T. Sakakibara, and K. Kindo, J. Phys. Soc. Jpn. **76**, 094709 (2007).

[23]H. Mitamura, R. Watanuki, K. Kaneko, N. Onozaki, Y. Amou, S. Kittaka, R. Kobayashi, Y. Shimura, I. Yamamoto, K. Suzuki, S. Chi, and T. Sakakibara, Phys. Rev. Lett. **113**, 147202 (2014).

[24]H. Ochimizu, T. Takamasu, S. Takeyama, S. Sasaki, and N. Miura, Phys. Rev. B **46**, 1986 (1992).

[25]N. Miura, R. G. Clark, R. Newbury, R. P. Starrett, and A. V. Skougarevsky, Physica B **194-196**, 1191 (1994).

[26]K. Sugiyama, F. Iga, M. Kasaya, T. Kasuya, and M. Date, J. Phys. Soc. Jpn. **57**, 3946 (1988).

[27]K. Okuda, S. Noguchi, A. Yamagishi, K. Sugiyama, and M. Date, Jpn. J. Appl. Phys., Part 1 **26**, L822 (1987).

[28]S. Badoux, W. Tabis, F. Laliberté, G. Grissonnanche, B. Vignolle, D. Vignolles, J. Bèard, D. A. Bonn, W. N. Hardy, R. Liang, N. Doiron-Leyraud, L. Taillefer, and C. Proust, Nature **531**, 16983 (2016).

[29]K. Sugiyama, H. Fuke, K. Kindo, K. Shimohata, A. A. Menovsky, J. A. Mydosh, and M. Date, J. Phys. Soc. Jpn. **59**, 3331 (1990).

[30]A. Kondo, J. Wang, K. Kindo, T. Takesaka, Y. Ogane, Y. Kawamura, T. Nishioka, D. T. H. Tanida, and M. Sera, J. Phys. Soc. Jpn. **80**, 013701 (2011).

[31]B. J. Ramshaw, K. A. Modic, A. Shekhter, Y. Zhang, E.-A. Kim, P. J. W. Moll, M. D. Bachmann, M. K. Chan, J. B. Betts, F. Balakirev, A. Migliori, N. J. Ghimire, E. D. Bauer, F. Ronning, and R. D. McDonald, Nat. Commun. **9**, 2217 (2018).

[32]W. Knafo, D. Aoki, D. Vignolles, B. Vignolle, Y. Klein, C. Jaudet, A. Villaume, C. Proust, and J. Flouquet, Phys. Rev. B **81**, 094403 (2010).

[33]W. Knafo, M. Vališka, D. Braithwaite, G. Lapertot, G. Knebel, A. Pourret, J.-P. Brison, J. Flouquet, and D. Aoki, J. Phys. Soc. Jpn. **88**, 063705 (2019).

[34]G. Machel and M. von Ortenberg, Physica B **211**, 355 (1995).

[35]H. Mitamura, PCT/JP2017/009539, 09 March 2017.

[36]H. Mitamura, PCT/JP2019/015560, 10 April 2019.

[37]R. Watanuki, T. Kobayashi, R. Noguchi, and K. Suzuki, J. Phys.: Conf. Ser. **150**, 042229 (2009).

[38]B. S. Shastry and B. Sutherland, Physica B & C **108**, 1069 (1981).

[39]T. Onimaru, K. T. Matsumoto, K. Umeo, T. Sakakibara, Y. Karaki, M. Kubota, and T. Takabatake, Phys. Rev. Lett. **106**, 177001 (2011).

[40]M. Matsushita, J. Sakaguchi, Y. Taga, M. Ohya, S. Yoshiuchi, H. Ota, Y. Hirose, K. Enoki, F. Honda, K. Sugiyama, M. Hagiwara, K. Kindo, T. Tanaka, Y. Kubo, T. Takeuchi, R. Settai, and Y. Ōnuki, J. Phys. Soc. Jpn. **80**, 074605 (2011).